LAKE FOREST COLLEGE

Senior Thesis

Predicting AM Canum Venaticorum Populations for LISA's mHz Gravitational Wave Observations

by

Dean Kousiounelos

22 April, 2025

The report of the investigation undertaken as a
Senior Thesis, to carry 2 courses of credit in
The Department of Physics

_____

Tara Natarajan
Krebs Provost & Vice
President for Academic Affairs;
Dean of the Faculty

Prof. Michael M. Kash, *Thesis Chair*

Dr. Seth Gossage, *Thesis Committee Member*

Prof. Veronika Walkosz, *Thesis Committee Member*

Prof. Elizabeth Fischer, *Thesis Committee Member*

ACKNOWLEDGEMENTS

I would like to express my gratitude toward my thesis committee for their excellent guidance and critique. I am grateful for Professor Michael M. Kash, whose guidance has led me down a fruitful path in physics and who has propelled me into the environs of thinking scientifically, selflessly preparing me with an abundance of tools to learn. This thesis wouldn't be possible without the generous donation of textbooks from Professor Kash. I also thank Dr. Seth Gossage, who took me on as a naive student and brought me far from where I started. He generously devoted much of his time to helping me refine my skills in computation and has been nothing short of a perfect role model for an astrophysicist. I am grateful to Dr. Vicky Kalogera for welcoming me into her group and providing an endless supply of inspiration upon which to build a strong foundation in research. Her leadership is something I strive to achieve one day. I am thankful to Professor Walkosz for always being willing to discuss obstacles, and to Professor Elizabeth Fischer for standing behind the decision to put my visualizations in this thesis. I also extend my gratitude to the Center for Interdisciplinary Exploration and Research in Astrophysics (CIERA) at Northwestern University for nurturing my research interests from a pre-undergraduate stage. The community has been everything I could have hoped for, and I am thankful for their collaboration with Lake Forest College on my senior thesis. I am grateful for my family and friends who have supported me along the way.

This research was supported in part through the computational resources and staff contributions provided for the Quest high-performance computing facility at Northwestern University, which is jointly supported by the Office of the Provost, the Office for Research, and Northwestern University Information Technology.

This research was supported in part by the Gordon and Betty Moore Foundation.

ABSTRACT

AM (Canum Venaticorum) CVn binaries are crucial verification systems for the upcoming **L**aser **I**nterferometer **S**pace **A**ntenna (LISA) mission as they emit gravitational waves at the mHz range $\left(0.3\text{mHz} < f_{\text{gr}} < 1\text{mHz}\right)$ and emit electromagnetic radiation in the optical and X-ray bands. Using a Binary Population Synthesis (BPS) simulation, POSYDON, we present an inference on the population and distribution of AM CVn type systems in a 10^6 galactic model to understand the abundance of low-frequency gravitational wave signals emitted from these binaries during LISA's first observing run. We seek to explain the various formation channels of these short-period binaries and create a large, open-source grid of binary stellar evolution simulations using **M**odules for **E**xperiments in **S**tellar **A**strophysics (MESA) for stars with $(0.8M_\odot < M_{\text{i}} < 8M_\odot)$ at solar metallicity ($Z = 0.0142$ dex) and an initial orbital period parameter range of (0.01 days $< P_{\text{orb}} < 1000$ days). We found $N = 39$ AM CVn systems out of our population, formed by the He WD channel. Our study points toward the necessity to update our models' α_{CE} parameter as well as consider several different magnetic braking prescriptions. With our results, we seek to refine the contribution of AM CVn binaries to the stochastic gravitational wave background (SGWB) and prepare for LISA's first observation.

CONTENTS

LIST OF FIGURES

LIST OF TABLES

NOMENCLATURE

AGB. Asymptotic Giant Branch.

AML. Angular Momentum Loss.

AMT. Angular Momentum Transport.

CO. Compact Object.

CV. Cataclysmic Variable.

CVn. Canum Venaticorum.

CVs. Cataclysmic Variable.

GR. Gravitational Radiation.

GW. Gravitational Waves.

HB. Horizontal Branch.

HeMS. Helium Main Sequence.

HMS. Hydrogen Main Sequence.

LISA. Laser Interferometer Space Antenna.

MB. Magnetic Breaking.

MESA. Modules for Experiments in Stellar Astrophysics.

MS. Main Sequence.

MT. Mass Transfer.

PMS. Post Main Sequence.

POSYDON. POpulation SYnthesis with Detailed binary-evolution simulatiONs.

RGB. Red Giant Branch.

RLO. Roche Lobe Overflow.

RLOF. Roche Lobe Overflow.

SGB. Sub-Giant Branch.

SGWB. Stochastic Gravitational Wave Background.

TOV. Tolman-Oppenheimer-Volkoff.

WD. White Dwarf.

ZAMS. Zero Age Main Sequence.

LIST OF VARIABLES

Variable	Description	First Appears
Stellar Structure Variables		
r	Radial distance from center	1.1
m	Mass enclosed within radius r	1.2
ρ	Density	1.2
P	Pressure	1.1
T	Temperature	1.9
L	Luminosity	1.9
ϵ	Nuclear energy generation rate	1.9
κ	Opacity	1.15
X_i	Mass fraction of nuclear species i	1.22
Z	Metallicity	1.22
μ	Mean molecular weight	1.24
v	Specific volume	1.12
ν	Specific heat capacity per unit mass	1.12
Binary Evolution Variables		
a	Orbital separation	1.46
a_i	Initial orbital separation	-
a_f	Final orbital separation	-
$a_{\text{pre-CE}}$	Orbital separation pre-common envelope	-
$a_{\text{post-CE}}$	Orbital separation post-common envelope	-
$\dot{a}$	Rate of change of orbital separation	1.47
$\dot{a}_{\text{wind}}$	Change in separation due to wind mass loss	-
$\dot{a}_{\text{tides}}$	Change in separation due to tides	-
$\dot{a}_{\text{GR}}$	Change in separation due to gravitational-wave radiation	-

Variable	Description	First Appears
c	Speed of light	1.58
e	Orbital eccentricity	1.47
$\dot{e}$	Rate of change of orbital eccentricity	1.47
J	Total angular momentum	1.54
J_{orb}	Orbital angular momentum	1.54
$\dot{J}_{\mathrm{orb}}$	Rate of change of orbital angular momentum	1.56
$\dot{J}_{\mathrm{gr}}$	Angular momentum loss from gravitational radiation	1.56
$\dot{J}_{\mathrm{ml}}$	Angular momentum loss from mass loss	1.56
$\dot{J}_{\mathrm{mb}}$	Angular momentum loss from magnetic braking	1.56
$\dot{J}_{\mathrm{ls}}$	Angular momentum exchange from spin-orbit coupling	1.56
M_1	Mass of primary/donor star	1.44
M_2	Mass of secondary/accretor star	1.44
$\dot{M}_1$	Mass loss rate of donor star	1.55
$\dot{M}_2$	Mass accretion rate of accretor star	1.55
$\dot{M}_{1,w}$	Wind mass loss rate from donor	1.55
$\dot{M}_{2,w}$	Wind mass loss rate from accretor	1.55
$\dot{M}_{\mathrm{RLOF}}$	Roche lobe overflow mass transfer rate	1.55
P_{orb}	Orbital period	1.58
q	Mass ratio (M_2/M_1)	1.48
R_{donor}	Radius of donor star	1.46
α_{CE}	Common envelope efficiency parameter	1.50
λ	Structure parameter for envelope binding energy	1.53
Φ	Effective gravitational potential	1.44
ω	Angular velocity (general)	1.44
ω_1	Rotational angular velocity of star 1	1.57
ω_2	Rotational angular velocity of star 2	1.57
ω_{orb}	Orbital angular velocity	1.57

Variable	Description	First Appears
ζ_{donor}	Mass-radius exponent for donor	1.49
ζ_L	Mass-radius exponent for Roche lobe	1.49

Chapter 1

INTRODUCTION

1.1 Overview

The Milky Way Galaxy contains approximately 100 billion stars, with binary systems extremely common throughout. Many stars in our galaxy orbit in pairs as binary stars, especially in globular clusters where stars of various ages form close relationships. Of those, the fraction that is low mass binary stars is $\approx 30 - 40\%$. The prevalence of binary systems creates a vast population of potential sources for ripples in space-time as these stars evolve.

Low mass stars (i.e, with masses between 0.4 solar masses and 8 solar masses) lack sufficient mass to end their lives as supernovae. Instead, they conclude their existence as white dwarfs (WDs) - dense, cooling remnants about the size of Earth but with a mass similar to our Sun. When these stars exist in close binary systems, they can form AM Canum Venaticorum (AM CVn) binaries. These are special star systems where a helium star and a white dwarf star orbit extremely close to each other, with one star transferring material to the other.

These AM CVn systems orbit each other at high speeds, creating radiation in the form of gravity we call gravitational waves. Einstein's theory of relativity predicted these waves, which were first directly detected in 2015 [1].

The gravitational wave frequency from AM CVn systems falls within a range that Earth-based detectors are not sensitive to (nHz to 0.1 mHz). The latest development of gravitational wave detectors, the Laser Interferometer Space Antenna (LISA) mission, a space-based detector, will support the detection of AM CVn within this frequency range. In a heliocentric orbit at a distance of 50 million km from Earth, the detector will have little interference between its 2.5 million km-long arms [2].

AM CVn binaries are valuable for LISA because they emit both gravitational waves and

light across different wavelengths. This dual emission makes them "verification binaries."

Understanding how these systems form and evolve requires extensive computer simulations run on powerful supercomputers. These calculations model thousands of possible scenarios for how stars might interact over billions of years. By comparing these simulations with actual observations, we can better predict how many AM CVn systems exist in our galaxy and how LISA might detect them. When operational, LISA will potentially revolutionize our understanding of these compact star systems and provide new insights into the gravitational wave landscape of our galaxy.

This research represents more than two years of dedicated work, requiring thousands of computational hours on Northwestern University's advanced super-computing system *Quest*. The simulation of these binary star systems involved processing large amounts of data and calculations to model stellar evolution across cosmic timescales. Each simulation run demanded significant computational resources, often running for multiple days to accurately represent the billions of years of stellar evolution. This computational effort was necessary to create a robust model that could predict the population and distribution of AM CVn systems, providing insights for the upcoming systems that the LISA mission can detect.

Hertzsprung–Russell diagram

Hertzsprung–Russell or temperature luminosity diagram. (Adapted from Goldberg, L. & Dyer, E. R. in *Science in Space*, L. V. Berkner & H. Odishaw, eds., McGraw-Hill Book Company, 1961.)
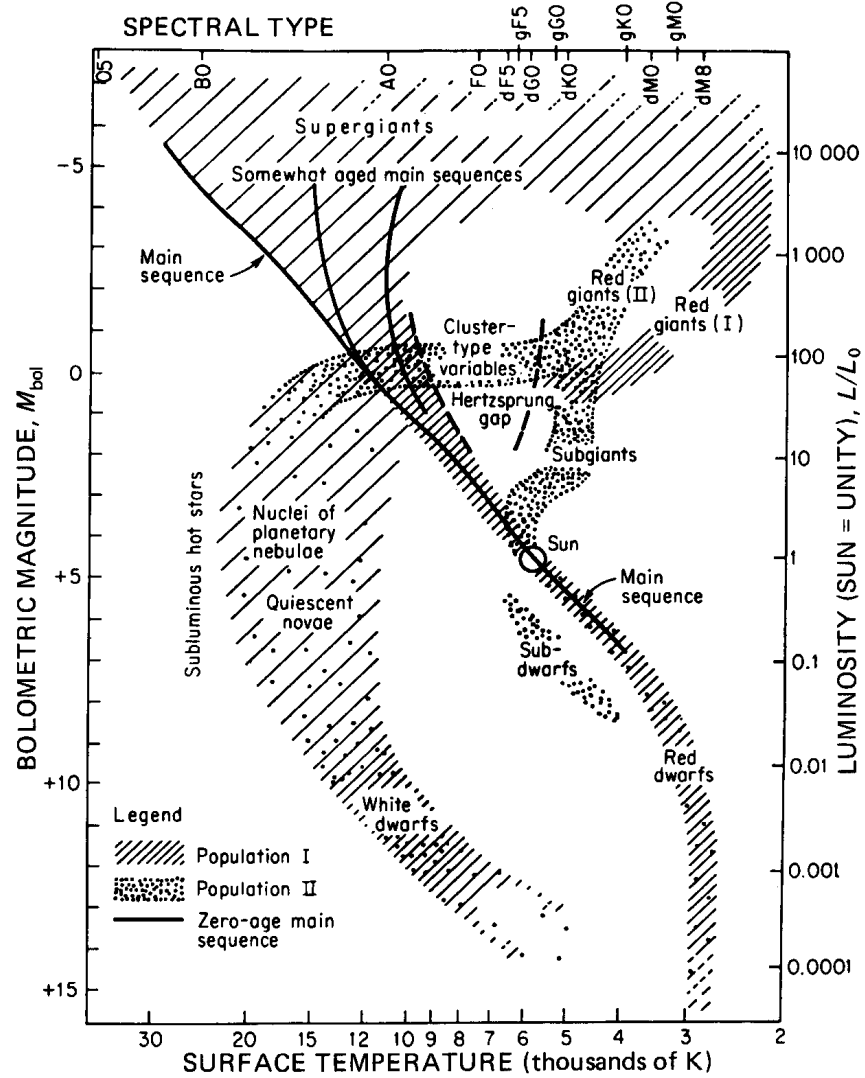
Figure 1.1: Hertzsprung-Russell Diagram adopted from [3].

1.2 Background

As we begin our search for a LISA source, our first step is to generally understand the evolution of an initially low-mass binary system to the point at which it will emit gravitational waves. We must first lay out a model of the stars we will evolve to create a foundation for later treatments of stellar evolution and binary stellar evolution. This section offers a quick overview of some of the general equations numerically solved in our simulations. For a more complete view of the equations used, please refer to [4–8]. It is important to note that the form of our stellar structure equations will be Lagrangian. The motivation for this is computational: the radius of a star changes drastically, whereas mass stays relatively stable during a star's life.

A Stellar Model

A star is a gaseous body, the pressure of which is in equilibrium with the inward force of gravity. The polytrope model is commonly used for a basic stellar structure model. It is based on the solution to the differential equation of hydrostatic equilibrium [9]:

$$\frac{1}{r^2}\frac{d}{dr}\left(\frac{r^2}{\rho(r)}\frac{dP}{dr}\right) = -4\pi G\rho(r). \tag{1.1}$$

Where P is the pressure, r is the radius from the center of the star, G is Newton's Gravitational Constant, and ρ is the density;. The family of solutions to this 2nd order ordinary differential equation is called the polytropic solutions and is of the form $P = k\rho^{\Gamma}$ where k is a constant, $\Gamma = 1 + 1/n$, and n is the **polytropic index**. A fully convective star, for example, is an $n = 1.5$ polytrope[1]. The model is based on these simplifying assumptions[2]:

1. The star is static.

2. The star is spherically symmetric.

3. The star is non-relativistic.

---

[1]Most polytrope models have $1 < n < 3$.

[2]Although we start with these assumptions, we will see later that certain stages of a binary evolution cause these assumptions to break down.
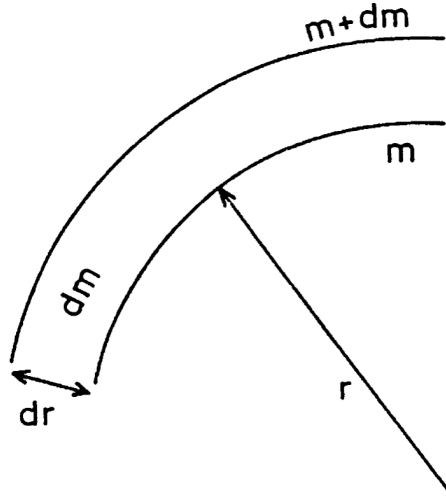
Figure 1.2: Schematic of a quadrant of the shell. Adopted from [8].

We begin with a thin spherical shell with infinitesimal thickness and a radius r from the center. For the infinitesimal mass in the shell, we have the **mass conservation equation**,

$$\frac{\partial m}{\partial r} = 4\pi r^2 \rho,$$ (1.2)

where ρ is density and m is a function of (r,t). The sum of the forces from pressure and the weight of the shell can be equated with the assumption that the system is in hydrostatic equilibrium[3]

$$\frac{\partial P}{\partial r} = -\frac{Gm}{r^2}\rho.$$ (1.3)

Re-arranging the independent variable m while using the inverse of the expression (1.2) we obtain:

$$\frac{\partial P}{\partial m} = -\frac{Gm}{4\pi r^4}.$$ (1.4)

This is the Lagrangian form of hydrostatic equilibrium. It is often the case that spherical stars have accelerated radial motion, and the mass elements have inertia. The equation of motion is given by

[3]For a first-principle derivation of Hydrostatic Equilibrium, refer to [10].

$$\frac{1}{4\pi r^2}\frac{\partial^2 r}{\partial t^2} = -\frac{\partial P}{\partial m} - \frac{Gm}{4\pi r^4}. \tag{1.5}$$

When the mass elements move radially at a constant velocity, we obtain equation 1.4 again. In the case that our star is relativistic, then our equation of hydrostatic equilibrium will take the form of the general *Tolman-Oppenheimer-Volkoff* (TOV) equation

$$\frac{\partial P}{\partial m} = -\frac{Gm}{r^2}\rho\left(1+\frac{P}{\rho c^2}\right)\left(1+\frac{4\pi r^3 P}{mc^2}\right)\left(1-\frac{2Gm}{rc^2}\right)^{-1}, \tag{1.6}$$

Where c is the speed of light. This prescription is used for a relativistic CO.

Gravitation

In a simple model, the gravitational field of our star is modeled by a Poisson equation:

$$\frac{1}{r^2}\frac{d}{dr}\left(r^2\frac{\partial\phi}{\partial r}\right) = 4\pi G\rho(r). \tag{1.7}$$

In simplifying this equation, only the radial component remains, leaving us with a single-order differential equation:

$$\frac{\partial\phi}{\partial r} = -\frac{Gm}{r^2}. \tag{1.8}$$

In later sections, our gravitational field is complicated by the presence of another star.

Conservation of Energy and Stellar Sources of Energy

As we build a picture of a detached single star, we must build a model for the conservation of energy as it travels from the star's center to the surface. Luminosity is denoted by $L(r)$ and $l(r)$ is the function of energies transported through the shells of the stellar interior by radiation, conduction, or convection (this depends on the type of star as well as its stage in evolution). These equations follow closely the derivation from [8]. Let us begin with the same spherical shell geometry as before. Our expression for energy is [4]

$$dl = 4\pi r^2\rho(r)\varepsilon dr, \tag{1.9}$$

---

[4] In our later discussion of the computer code `MESA`, this form of the equation is numerically solved for the Luminosity of the star (replace $l \rightarrow L$).

where ε is the nuclear energy released and depends on temperature, density, and abundance. With our desire to keep our expressions in terms of the mass element, we can write this expression as such

$$\frac{\partial l}{\partial m} = \varepsilon,$$
(1.10)

where for non-stationary shells (such that there is mixing between them) and the accounting for the origin of neutrinos, we rewrite such that

$$\frac{\partial l}{\partial m} = \varepsilon - \varepsilon_\nu + \varepsilon_g,$$
(1.11)

where ε_ν is the energy taken in the form of neutrinos, and

$$\varepsilon_g = -c_P \frac{\partial T}{\partial t} + \frac{\delta}{\rho} \frac{\partial P}{\partial t},$$

where

$$\delta = \frac{T}{v} \left(\frac{\partial v}{\partial T} \right)_P$$

c_P is the specific heat capacity per unit mass, $\left(\frac{\partial u}{\partial T} \right)_P + \left(\frac{\partial v}{\partial T} \right)_P$

v is the specific volume per unit mass, $1/\rho$.

By substitution, we arrive at:

$$\frac{\partial l}{\partial m} = \varepsilon_n - \varepsilon_\nu - c_P \frac{\partial T}{\partial t} + \frac{\delta}{\rho} \frac{\partial P}{\partial t}.$$
(1.12)

Energy transport

Beginning from the temperature gradient $\frac{dT}{dr}$ and the hydrostatic equation (1.3), we can obtain

$$\frac{dT}{dm} = \frac{dT}{dP} \frac{dP}{dm}.$$
(1.13)

By substituting equation (1.4) into the right hand side of (1.13), and utilizing the adiabatic pressure gradient $\nabla_{\text{ad}} = \left(\frac{P}{T}\frac{dT}{dP}\right)_s$, we come to the transport expression

$$\frac{\partial T}{\partial m} = -\frac{GmT}{4\pi r^4 P}\nabla. \tag{1.14}$$

For radiative transport,

$$\nabla = \nabla_{rad} = \frac{3}{16\pi acG}\frac{lP\kappa}{mT^4}. \tag{1.15}$$

Where κ is the stellar opacity. For convective transport: ∇ is calculated from mixing-length theory (MLT), with $\nabla \approx \nabla_{ad}$ in the deep interior.

Radiative and Convective Envelopes

Stars can be characterized by whether their outer envelopes, the layers below the photosphere, are radiative or convective. Different regions of the star react differently during stellar evolution.
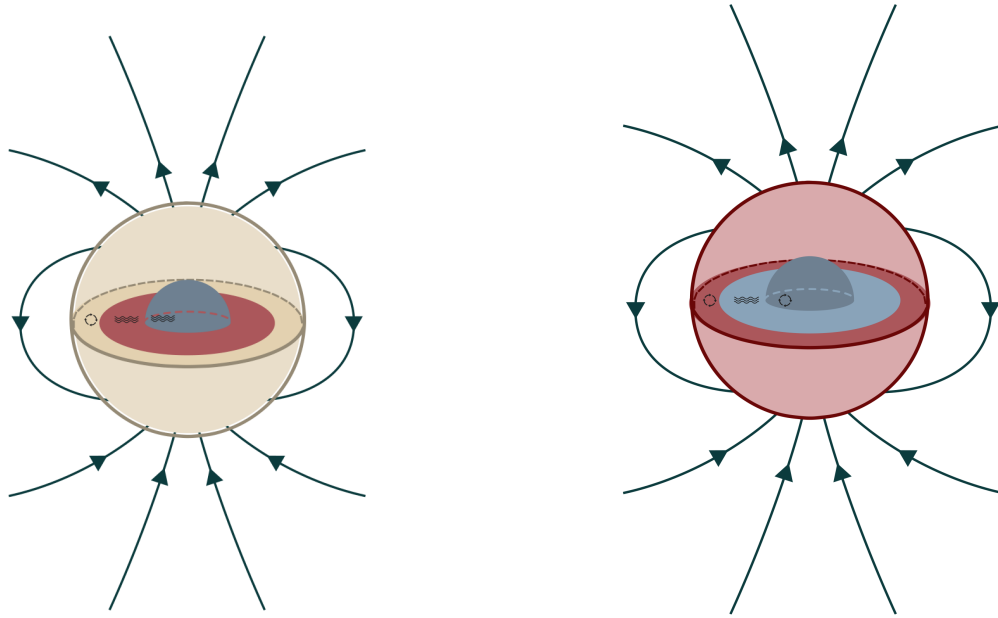
Figure 1.3: Two artistic renditions of stars with magnetic field lines and shells. Shells can be convective or radiative.

Radiative Envelopes

Stars with $M \gtrsim 1.41 M_\odot$ [11] typically have radiative envelopes where energy is transported primarily by radiation to the outer layers. In this regime where little mixing of material happens between layers, the temperature gradient will follow $\nabla = \nabla_{\mathrm{rad}}$, thus our transport equation looks like

$$\frac{\partial T}{\partial m} = -\frac{3}{64\pi^2 ac} \frac{kl}{r^4 T^3}. \tag{1.16}$$

Making the substitution ($\sigma = ac/4$) as in [8], and utilizing $\dfrac{\partial T}{\partial P} = \dfrac{\partial T}{\partial m} \dfrac{\partial m}{\partial P}$ we obtain[5]

$$\frac{\partial T}{\partial P} = \frac{3}{64\pi\sigma G} \frac{kl}{T^3 m}. \tag{1.17}$$

As a radiative envelope approaches the surface, the temperature gradient typically becomes shallower (smaller ∇).

Convective Envelopes

Stars with $M \lesssim 1.32 M_\odot$ [11] typically have convective envelopes where energy is transported by large-scale convective motions in the outer layers. In this regime, the temperature gradient approaches $\nabla \approx \nabla_{\mathrm{ad}}$ in the deeper parts of the envelope, and there is significant mixing of material throughout the convective region. Surface abundances can be altered by dredge-up of processed material from the interior. The process of mixing, which occurs between the hydrogen-burning shell and the outer convective envelope of a star, is called Thermohaline mixing and affects the chemical yields of low-mass stars. [12]. Convective envelope depth varies with stellar mass. For instance, for our Sun ($M = 1 M_\odot$), the convective envelope extends inward to about 70% of the solar radius. However, for $M \lesssim 0.35 M_\odot$ [13], stars are fully convective. The temperature gradient in a deep convective envelope follows:

Chemical Compositions

Consider a unit volume with number density n_i of nuclei of type i with mass m_i. The mass fraction is defined as $X_i = \frac{n_i m_i}{\rho}$. The rate of change of n_i is the difference between the

---

[5]We choose this notation because m varies very little in the envelope.

production rate $\sum_j r_{ji}$ (transforming species j into species i) and the destruction rate $\sum_k r_{ik}$ (reactions transforming species i into species k). Thus:

$$\frac{\partial n_i}{\partial t} = \sum_j r_{ji} - \sum_k r_{ik} \tag{1.18}$$

$$\frac{\partial}{\partial t}\left(\frac{\rho X_i}{m_i}\right) = \sum_j r_{ji} - \sum_k r_{ik} \tag{1.19}$$

$$\frac{\rho}{m_i}\frac{\partial X_i}{\partial t} = \sum_j r_{ji} - \sum_k r_{ik} \tag{1.20}$$

Each X_i is the abundance of species i.

$$X \equiv X_{\mathrm{H}}, Y \equiv X_{\mathrm{He}} \tag{1.21}$$

Z is the metallicity of the stellar composition and includes elements heavier than Hydrogen and Helium, such as Carbon, Nitrogen, Oxygen, etc.[6]

A star's chemical composition is governed by nuclear reactions, which transform one nuclear species into another. The rate of change of the abundance X_i of each nuclear species is described by:

$$\frac{\partial X_i}{\partial t} = \frac{m_i}{\rho}\left(\sum_j r_{ji} - \sum_k r_{ik}\right), \quad i = 1, \ldots, I \tag{1.22}$$

Solving for $\frac{\partial X_i}{\partial t}$ gives the result. This equation tracks how nuclear reactions change the chemical composition throughout the star's evolution. In summary, a full set of differential

---

[6]"Metallicity" does not refer to a metal (electrically conducting solid).

equations based on our initial assumptions is:

$$
\left\{
\begin{array}{l}
\dfrac{\partial r}{\partial m} = \dfrac{1}{4\pi r^2 \rho} \\[2ex]
\dfrac{\partial P}{\partial m} = -\dfrac{Gm}{4\pi r^4} \\[2ex]
\dfrac{\partial l}{\partial m} = \varepsilon_n - \varepsilon_\nu - c_P \dfrac{\partial T}{\partial t} + \dfrac{\delta}{\rho} \dfrac{\partial P}{\partial t} \\[2ex]
\dfrac{\partial T}{\partial m} = -\dfrac{GmT}{4\pi r^4 P} \nabla \\[2ex]
\dfrac{\partial X_i}{\partial t} = -\dfrac{m_i}{\rho} \left(\sum_j r_{ji} - \sum_k r_{ik} \right) \quad i = 1, \ldots, I
\end{array}
\right\}
$$

These equations (namely 1.12, 1.14-1.17, 1.24) are supplemented by expressions that describe the material properties[7]:

$$\rho_{eq} = \rho_{eq}(P, T, X_i) \quad \text{(equation of state)} \tag{1.23}$$

$$\varepsilon_n = \varepsilon_n(P, T, X_i) \quad \text{(nuclear energy generation)} \tag{1.24}$$

$$\varepsilon_\nu = \varepsilon_\nu(P, T, X_i) \quad \text{(neutrino energy loss)} \tag{1.25}$$

$$\kappa = \kappa(P, T, X_i) \quad \text{(opacity)} \tag{1.26}$$

The energy transport occurs through different mechanisms, reflected in the value of $\nabla \equiv \dfrac{d \ln T}{d \ln P}$. The solution of these equations, with appropriate boundary conditions and constitutive relations, provides a complete description of the internal structure of a star at a given moment in time.

Degenerate Matter

The pressure of a low-mass stellar remnant is partly supported by the **electron degeneracy pressure**. Stars with mass below $\approx 1.44 M_\odot$ (The Chandrasekhar limit) retain themselves free of gravitational core collapse as this pressure halts the process by exerting a force against gravity–maintaining stability. This pressure[8] is partially caused by the quantum mechanical *anti-symmetrization requirement* for the wave function of identical fermions [14].

---

[7]These are referred to in some textbooks as the **constitutive relations**.
[8]sometimes also referred to as exclusion pressure.

$$P_e = \frac{(3\pi^2)^{2/3}\hbar^2}{5m_e}\rho^{5/3}$$

(1.27)

Where m_e is the mass of the electron, and ρ_e is the number of electrons per unit volume.

Detached Stellar Evolution

In this section, we will discuss what occurs to stellar structure when hydrostatic equilibrium is lost and pressure opposes the pull of gravity. Most of the processes that occur in a star, which we enlightened upon in the previous chapter, are affected by this pressure disruption. Stars shine mainly due to nuclear fusion and a radiative loss of energy from gravitational contraction. Fluctuations in their luminosity are indications of their evolutionary paths. These paths can be predicted with the virial theorem, which tells us that as stars radiate energy and attempt to cool, they contract and heat up. The fundamental property that stars have negative heat capacity [15] drives stellar evolution. It is important to state that we don't begin our conversation at stellar formation, but rather at the Zero Age Main Sequence (ZAMS). This is the beginning of the Main Sequence (MS) which is, by far, the longest section of a star's life. during this time, the star goes through relatively small changes to its stellar structure.

single star		
initial mass	He-core mass	final remnant
$\lesssim 2.0\,M_\odot$	$\approx 0.6\,M_\odot$	CO white dwarf
$2.0 - 6\,M_\odot$	$0.6 - 1.7\,M_\odot$	CO white dwarf
$6 - 8\,M_\odot$	$1.7 - 2.2\,M_\odot$	ONe white dwarf
$8 - 10\,M_\odot$	$2.2 - 3.0\,M_\odot$	neutron star
$10 - 25\,M_\odot$	$3.0 - 10\,M_\odot$	neutron star
$\gtrsim 25\,M_\odot$	$> 10\,M_\odot$	black hole

Table 1.1: Stellar evolution outcomes based on initial mass and maximum helium core mass for single stars at solar metallicity [15]

Our conversation of stellar evolution is limited to initially low-mass to intermediate-mass stars such as our sun (0.8-8 $M_\odot$). Thus, we will *not* discuss the evolution of supergiants and hone in on the evolution of changing internal features of these low-mass stars. The range

of initial mass we are dissecting is under that which will form into neutron stars and is free of any core-collapse or supernovae stages.

Nuclear Energy Sources in Stellar Evolution

Nuclear reactions serve as the primary energy source for stars throughout most of their lifetime. The energy generation rate (ε_n) in the energy conservation equation (1.12) depends critically on the specific nuclear processes occurring in different evolutionary phases:

1. **Hydrogen Burning**: The fusion of four hydrogen nuclei into one helium nucleus occurs through two main processes:

   - *Proton-Proton (PP) Chain*: Dominates in stars with M $\lesssim$ 1.3 $M_\odot$ and T $\lesssim$ 1.5 $\times 10^7$ K. This reaction forms a deuterium nucleus from two protons. The key reactions are:

   $$^1_1\text{H} + ^1_1\text{H} \rightarrow ^2_1\text{H} + e^+ + \nu_e \tag{1.28}$$

   $$^2_1\text{H} + ^1_1\text{H} \rightarrow ^3_2\text{He} + \gamma \tag{1.29}$$
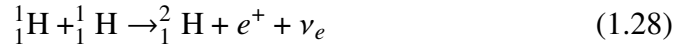
   followed by either $^3_2\text{He} + ^3_2\text{He} \rightarrow ^4_2\text{He} + 2^1_1\text{H}$ (PP-I branch) or alternate branches involving ^7Be and ^8B.[10]

   - *CNO Cycle*: Dominates in stars with M $\gtrsim$ 1.3 $M_\odot$ due to their higher core temperatures. Carbon, nitrogen, and oxygen serve as catalysts in a cyclic process[10]:

   $$^{12}_6\text{C} + ^1_1\text{H} \rightarrow ^{13}_7\text{N} + \gamma \tag{1.30}$$

   $$^{13}_7\text{N} \rightarrow ^{13}_6\text{C} + e^+ + \nu_e \tag{1.31}$$

   $$^{13}_6\text{C} + ^1_1\text{H} \rightarrow ^{14}_7\text{N} + \gamma \tag{1.32}$$

   $$^{14}_7\text{N} + ^1_1\text{H} \rightarrow ^{15}_8\text{O} + \gamma \tag{1.33}$$

   $$^{15}_8\text{O} \rightarrow ^{15}_7\text{N} + e^+ + \nu_e \tag{1.34}$$

   $$^{15}_7\text{N} + ^1_1\text{H} \rightarrow ^{12}_6\text{C} + ^4_2\text{He} \tag{1.35}$$

The energy generation rate for hydrogen burning has a temperature dependence and the CNO cycle dominates at higher temperatures.

2. **Helium Burning**: After hydrogen exhaustion and core contraction raises temperatures to $\sim 10^8$ K, helium burning begins through the triple-alpha process:

$$^4\text{He} +^4 \text{He} \rightarrow^8 \text{Be} \tag{1.36}$$

$$^8\text{Be} +^4 \text{He} \rightarrow^{12} \text{C} + \gamma \tag{1.37}$$

followed by $^{12}\text{C} +^4 \text{He} \rightarrow^{16} \text{O} + \gamma$ for some fraction of the carbon.

The triple-alpha process has an extremely strong temperature dependence, which contributes to the explosive nature of the helium flash in low-mass stars. For low-mass stars ($M \lesssim 8M_\odot$), evolution typically stops after helium burning, leaving a carbon-oxygen core that cools to become a white dwarf. [9]

The nuclear energy generation rate can be expressed generally as:

$$\varepsilon_n = \sum_i \varepsilon_i = \sum_i \frac{Q_i}{m_i m_j} \rho X_i X_j \langle \sigma v \rangle_i \tag{1.38}$$

where Q_i is the energy released per reaction, X_i and X_j are mass fractions of the reacting nuclei, and $\langle \sigma v \rangle_i$ is the reaction rate, which depends strongly on temperature. The temperature dependence creates distinct burning shells and contributes to the structural changes observed during stellar evolution.

Simplifications Based on Timescales

The large separation between these timescales allows for important simplifications in stellar evolution calculations:

- Since τ_{dyn} is so short, stars maintain hydrostatic equilibrium for most of their evolution, except during collapse or explosion phases.

---

[9]However, it's worth noting that more massive stars continue through carbon, neon, oxygen, and silicon burning, eventually forming an iron core.

- When a star evolves on the nuclear timescale (τ_{nuc}), the time derivatives in the energy equation can be neglected, giving the simplified form:

$$\frac{\partial l}{\partial m} = \varepsilon_n - \varepsilon_\nu \qquad (1.39)$$

This represents a star in "complete equilibrium" (both hydrostatic and thermal).

- During rapid phases of evolution, when a star evolves on the thermal timescale (τ_{KH}), the full energy equation with time derivatives must be used, but nuclear composition changes may still be small.

Zero Age Main Sequence

Low-mass stars begin their life on the main sequence fusing hydrogen into helium in their cores through the proton-proton (pp) chain or CNO cycle. The CNO cycle, which is relatively a small contribution during the main sequence, begins to dominate at a stellar core temperature of 14×10^6 K. The CNO cycle becomes the primary source of energy for stars with $M > 1.5 M_\odot$. During this time, the star is changing on the nuclear timescale τ_n where it is burning through its nuclear fuel.

$$\tau_{\mathrm{nuc}} = 10^{10} \left(\frac{M}{M_\odot} \right)^{-2.5} \qquad (1.40)$$

This is the longest phase of stellar evolution, with lifetimes ranging from $\sim 10^{10}$ years for a 1 $M_\odot$ star to $\sim 10^8$ years for an 8 $M_\odot$ star.
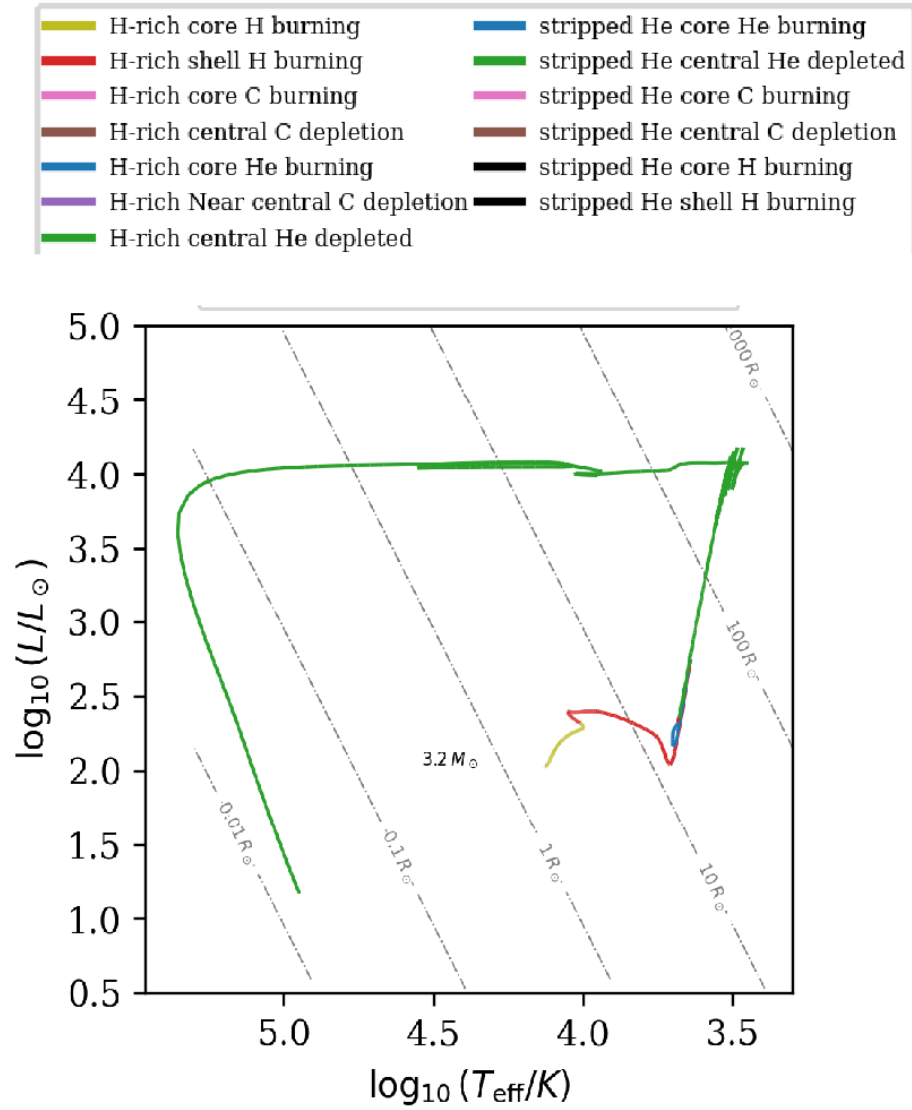
Figure 1.4: Hydrogen Main Sequence stellar track of of $3.2 M_\odot$ star. The Main Sequence is the region up until central He depleted.

Main sequence stars are classified according to their spectral characteristics, which correlate with their surface temperature. The classification system, ordered from hottest to coolest, consists of:

Stellar Classification

Table 1.2: Henry Draper (HD) spectral classification[3]

Stellar class	Class characteristics
O	(Blue-violet) Hot stars with He II absorption
B	(Blue-white) He I absorption; H developing later
A	(White) Very strong H, decreasing later; Ca II increasing
F	(Yellow-white) Ca II stronger; H weaker; metals developing
G	(Yellow) Ca II strong; Fe and other metals strong; H weaker
K	(Orange) Strong metallic lines; CH and CN bands developing
M	(Red) TiO bands developing strongly

Table 1.3: Table of main-sequence stellar parameters[3]

Stellar class	Radius, $R/R_\odot$	Mass, $M/M_\odot$	Luminosity, $L/L_\odot$	Temp. (K)	Examples
O2	12	100	800,000	50,000	Bl 253
O6	9.8	35	180,000	38,000	Theta Orionis C
B0	7.4	18	20,000	30,000	Phi Orionis
B5	3.8	6.5	800	16,400	Pi Andromedae A
A0	2.5	3.2	80	10,800	Alpha Coronae Borealis A
A5	1.7	2.1	20	8,620	Beta Pictoris
F0	1.3	1.7	6	7,240	Gamma Virginis
F5	1.2	1.3	2.5	6,540	Eta Arietis
G0	1.05	1.10	1.26	5,920	Beta Comae Berenices
G2	1	1	1	5,780	Sun
G5	0.93	0.93	0.79	5,610	Alpha Mensae
K0	0.85	0.78	0.40	5,240	70 Ophiuchi A
K5	0.74	0.69	0.16	4,410	61 Cygni A
M0	0.51	0.60	0.072	3,800	Lacaille 8760
M5	0.18	0.15	0.0027	3,120	EZ Aquarii A
M8	0.11	0.08	0.0004	2,650	Van Biesbroeck's star
L1	0.09	0.07	0.00017	2,200	2MASS J0523−1403

Helium Main Sequence (HeMS)

The Helium main sequence is an evolutionary track that contains mostly He with He burning in the core. The HeMS is to the far left of the HMS track on the Hertzsprung-Russell Diagram (See appended Diagram). Differences in mean molecular weight cause a greater luminosity and smaller radius for a given stellar mass–as compared to the HMS [8]. Due to radiation pressure, the HeMS star has an increased convective core.

Red Giant Branch (RGB)

After hydrogen is exhausted in the core, nuclear burning[10] shifts to a shell around a helium core. The core contracts and heats while the envelope expands dramatically, cooling the surface. The star ascends the Red Giant Branch (RGB), increasing in luminosity while decreasing in effective temperature. The helium core becomes electron-degenerate for stars below ~2.0 $M_\odot$[11].

| Mass | RGB | Core | $\text{RGB}^1_{\text{foot}}$ | | | Core | $\text{RGB}^2_{\text{end}}$ | | |
| | | | T_{eff} | Radius | Lum. | | T_{eff} | Radius | Lum. |
($M_\odot$)	(MYrs)	mass	(K)	($R_\odot$)	($L_\odot$)	mass	(K)	($R_\odot$)	($L_\odot$)
0.6	2,500	0.10	4,634	1.2	0.6	0.48	2,925	207	2,809
1.0	760	0.13	5,034	2.0	2.2	0.48	3,140	179	2,802
2.0	25	0.25	5,220	5.4	19.6	0.34	4,417	23.5	188
5.0	0.3	0.83	4,737	43.8	866.0	0.84	4,034	115	3,118

Table 1.4: Red Giant Branch Evolution Table [16, 17]. [1] The foot of the RGB is the end of CNO burning in the shell and at the very beginning of the RGB. [2]. The end of the RGB is when Helium ignition begins.

Helium Flash

(for M ≲ 2.0 $M_\odot$): In low-mass stars, helium ignition occurs under degenerate conditions, leading to a thermal runaway called the helium flash. This occurs at the tip of the RGB when the core reaches ~10^8 K. The flash doesn't manifest as a visible explosion but rapidly lifts the degeneracy, allowing for core helium fusion to begin.

---

[10]When we say burning, we refer to the fusion of an element into another.

[11]For stars above ~ 2.0$M_\odot$, the helium flash does not occur and the star continues to evolve, forming a loop (*blue loops*) back to the RGB or onto the AGB. For stars massive enough that are outside of the scope of this thesis, they may also supernovae.
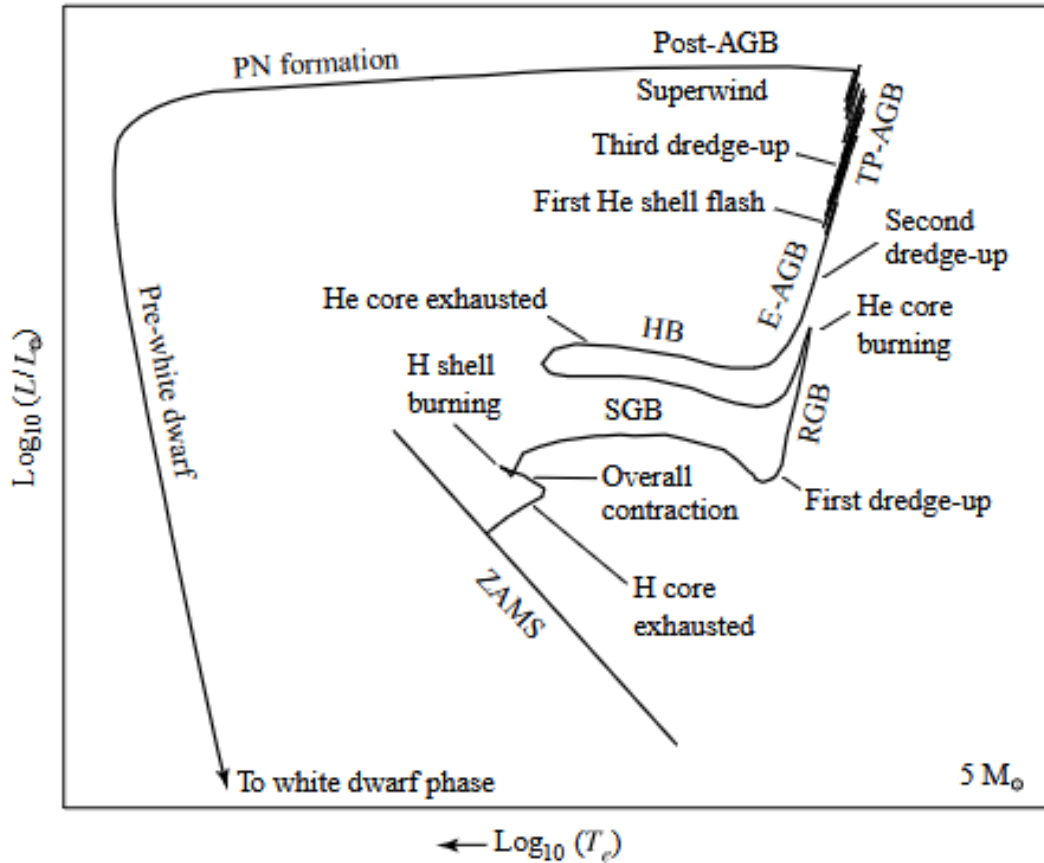
Figure 1.5: Schematic of a stellar evolution track for a 5 $M_\odot$ star. This figure shows the ZAMS, Helium Flash, HB, RGB, AGB evolution, as well as PN and WD phases. Adopted from [10] Figure 13.5.

Horizontal Branch (HB)

After the helium flash and steady helium ignition, the star stabilizes on the horizontal branch, burning helium in the core while hydrogen continues to burn in a surrounding shell. The star now has a higher temperature and lower luminosity than at the RGB tip.

Asymptotic Giant Branch (AGB)

When helium is exhausted in the core, the star develops a degenerate carbon-oxygen core with helium and hydrogen burning shells that surround it. The star expands again and ascends the AGB, similar to the RGB but at a higher luminosity. Stars around 0.5 to 8.0 $M_\odot$ typically enter the AGB phase at their later evolution. Thermal pulses occur due to instabilities in the helium-burning shell, leading to dredge-up events that bring processed material to the surface. Ultimately, this dredge-up leads to higher opacity in the outer

layer where particles are ionized, trapping radiation. The star responds by expanding, the recombined ionized particles cause the opacity decreased again and the star contracts. This cycle of ionization, expansion, recombination, and contraction is characterized by photometric variability with periods of 100–1000 days. The low surface gravity for stars on the AGB phase, and induced shock waves in the extended stellar atmosphere from this process, contribute to atmospheric levitation and ultimately to mass loss as the particles sail on a stellar wind away from the star [18].

Planetary Nebulae (PN)

For stars $< 8.0 M_\odot$, that have evolved through the AGB, there is a thick circumstellar envelope which eventually is ejected causing a large drop off of stellar mass. This ejected envelope of Hydrogen and Helium shells ultimately leaves behind the degenerate remnant star, a bare carbon-oxygen Core[12].

White Dwarf (WD)

The final stage is a white dwarf – the exposed degenerate carbon-oxygen core. With no nuclear energy sources, the white dwarf slowly cools over billions of years. Its structure is supported by electron degeneracy pressure rather than thermal pressure.

Binary Stellar Evolution

1.3 Binary Stellar Evolution

Unlike detached, single-star evolution, binary stellar evolution appends some complications to the stellar structure by coupled evolutionary dynamics. Such dynamics, mass transfer (MT) and angular momentum loss and transport (AML, AMT) change the timescale of evolution and each introduces a slew of mechanics which ultimately contributes to a short period binary which produces detectable gravitational waves [5]. This section introduces the complications of binary stellar evolution and the types of binary systems which are of

---

[12]This "Planetary Nebulae" does not have anything to do with planet formation but was misnamed by early astronomers due to its dusty, disk like appearance.

special interest for this thesis, and which we have been building up to over the previous chapter.

Celestial Mechanics of Two Bodies

Mass Transfer

In short-period binaries, when the donor star[1] evolves through the RGB, it overfills its Roche lobe. The Roche lobe is the region where there is constant effective gravitational potential, Φ, (effective potential per unit mass) given by:

$$\Phi = -G\left(\frac{M_1}{s_1} + \frac{M_2}{s_2}\right) - \frac{1}{2}\omega^2 r^2 \tag{1.41}$$

where M_1 and M_2 are the mass of the stars, and ω is the classical angular velocity, and s_1 and s_2 are distances from the respective star centers [10]
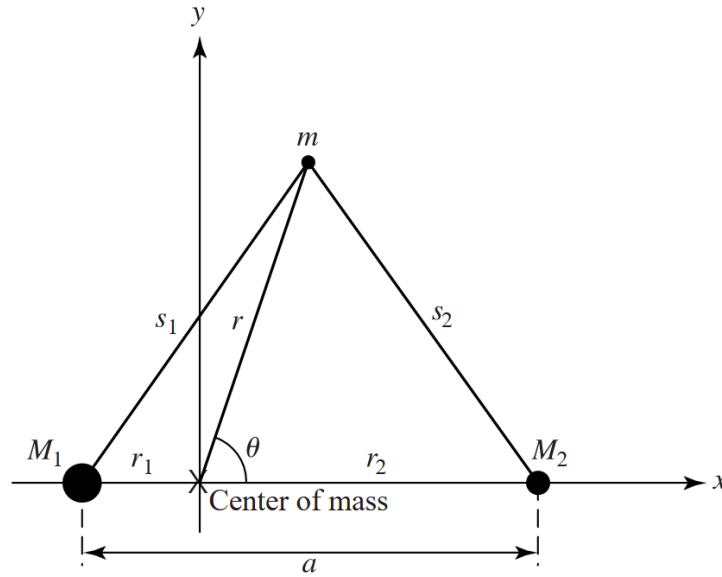
Figure 1.6: Diagram of coordinate system adopted from [10], Figure 18.1.

The x component of force on a test mass at rest on the x-axis is of the form:

$$F_x = -\frac{dU}{dx} = -m\frac{d\Phi}{dx} \tag{1.42}$$

where U is the gravitational potential energy. Points where there is no force on the test mass are Lagrangian points (denoted by ℓ_1). When the donor star's radius passes ℓ_1, it overfills its

Roche Lobe and begins transferring mass into the potential well of the other star, creating an accretion disk.
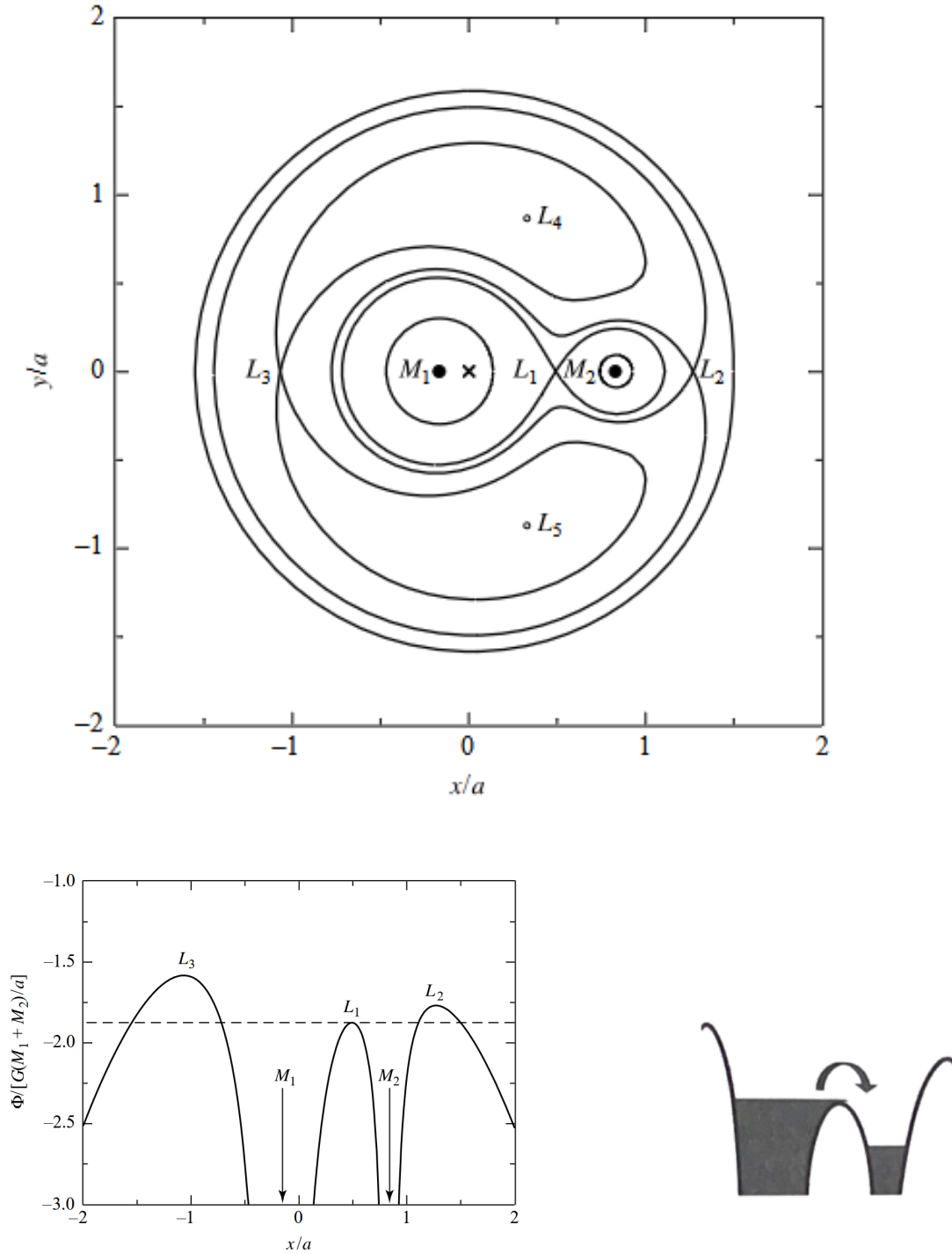
Figure 1.7: Equipotential surface of a binary system with the Lagrange points plotted. Adopted from [10] Figure 18.3 (Above). Side slice of the equipotential surface showing the potential wells. Adopted from [10] Figure 18.2 (Below Left). The "overflow" of mass from one potential well to another signifying mass transfer. Adopted from [19] Figure 4.4 (Below Right).

The boundary at which Roche-lobe overflow (RLO) begins is when the radius of the donor star R_{Donor} is greater than

$$\ell_1 = a \left[0.500 - 0.227 \log_{10} \left(\frac{M_2}{M_1} \right) \right] \tag{1.43}$$

where a is the semi-major axis of the orbit (separation distance). The relationship for the time evolution of the orbital separation is [19]

$$\frac{\dot{a}}{a} = 2 \frac{\dot{J}_{\text{orb}}}{J_{\text{orb}}} - 2 \frac{\dot{M}_1}{M_1} - 2 \frac{\dot{M}_2}{M_2} + \frac{\dot{M}_1 + \dot{M}_2}{M_1 + M_2} + \frac{e \dot{e}}{(1 - e^2)}, \tag{1.44}$$

were a is the orbital separation, $\dot{a}$ is the rate of change of the orbital separation, $\dot{M}$ is the rate of change of mass, e is the eccentricity, and J is the orbital angular momentum. For $e = 0$, our expression looks like

$$\frac{\dot{a}}{a} = -2 \frac{\dot{M}_1}{M_1} \left(1 - \frac{1}{q} \right). \tag{1.45}$$

q is the mass ratio of the companion star to the donor star. We assume that the RLO is conservative, in which the total orbital M and J remain constant. In this regime, when M_1[13] is larger than M_2 ($q < 1$), we can see that the orbit will shrink under mass transfer, as the rate of change of the orbital separation is negative [20].

Mass transfer is a necessary aspect of binary stellar evolution. Wether or not the transfer of mass is a stable process is critical for the formation of short-period CO binaries. The outcome of mass transfer directly contributes to the increase in orbital separation (for stable mass transfer) and shorter orbital separation (unstable mass transfer). When mass transfer is stable, it occurs on either the nuclear or thermal timescale of the donor star. A simple criterion for stable mass transfer is

$$\zeta_{\text{donor}} = \frac{\partial \ln R_2}{\partial \ln M_2} \quad \zeta_{\text{L}} = \frac{\partial \ln R_L}{\partial \ln M_2}, \tag{1.46}$$

where ζ_{donor} and ζ_{L} are exponents for the power-law fits for $R \approx M^{\zeta}$. At the onset of RLO, $R_2 = R_L$ (R_L is the Roche lobe radius). If $\zeta_{\text{L}} \leq \zeta_{\text{donor}}$, the system is considered stable. The mass transfer rate is highly dependent on the response of the donor star to mass loss, which

---

[13] $\dot{M}_1$ is a negative quantity.

differs significantly between stars with radiative and convective envelopes [21]. For systems where the donor star has a radiative envelope (also known as Case A RLO), the star's radius will shrink, maintaining stability. For stars with a convective envelope[14], the response to mass loss is such that the star expands while the Roche-lobe shrinks, creating unstable, runaway mass transfer. The quasi-adiabatic critical mass ratio, q_{qad}, is the lowest value of q[15] at the onset of Roche-lobe overflow (RLOF) for which a complete mass transfer phase can be simulated without the mass-transfer rate exceeding the critical thermal mass-transfer rate, $\dot{M}_{th,crit}$. This $\dot{M}_{th,crit}$ represents the maximum of $\dot{M}_{th(m)}$, the minimum mass-loss rate needed to strip outer stellar layers down to a mass coordinate m faster than they can thermally readjust [22]. According to the quasi-adiabatic criterion, unstable mass transfer occurs when the mass-loss rate ($\dot{M}_d$) surpasses $\dot{M}_{th,crit}$, leading to a fully adiabatic response from the donor star. For $q < q_{qad}$, mass transfer is unstable and ultimately leads to common envelope evolution.

Common Envelope Evolution

If mass transfer becomes unstable, the donor star may expand beyond ℓ_2, resulting in a common envelope (CE) phase. During this phase, the companion star orbits within the envelope of the donor, where it experiences strong drag forces that rapidly reduce the orbital separation [23]. This orbital energy is transferred to the envelope, facilitating orbital shrinkage. The efficiency of orbital shrinkage during CE is parameterized by the common envelope efficiency parameter α_{CE}, defined as:

$$\alpha_{CE} = \frac{\Delta E_{bind}}{\Delta E_{orb}} \quad \text{where} \quad 0 < \alpha_{CE} < 1 \tag{1.47}$$

where ΔE_{bind} is the binding energy of the ejected envelope and ΔE_{orb} is the change in orbital energy [23] [19]. α_{CE} is usually between 0 and 1, yet can be greater than 1 if the CE has

---

[14]for more depth on the stability and instability of mass transfer, read [22].

[15]in this case q is defined as $\frac{M_2}{M_1}$
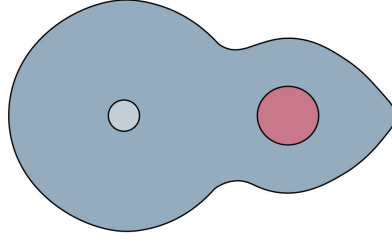
Figure 1.8: A simplified rendition of common envelope [26].

energy transferred to it from more than just the orbital energy [24]. E_{bind} is given by

$$E_{\text{bind}} = \int_{M_{\text{core}}}^{M_{\text{donor}}} \left(-\frac{GM(r)}{r} + \alpha_{\text{th}}U \right) dm \tag{1.48}$$

where $M(r)$ is a function describing the amount of mass interior to the position. The location of M_{core} is the known as the bifurcation point, which is the isolated point at the intersection of the ejected envelope and the core. U is the specific internal energy of the gas and α_{th} is the fraction of U that can be used for the ejection of the envelope. ΔE_{orb} is defined as

$$\Delta E_{\text{orb}} = -\frac{GM_{\text{core}}M_1}{2a} + \frac{GM_{\text{donor}}M_1}{2a_0}, \tag{1.49}$$

where a_0 and a are initial and final orbital separations at the onset of RLO and at the end of CE. Physically, the α_{CE} encapsulates a rather complex processes including energy transport, radiation losses, and recombination energy contribution during the rapid CE phase [25]. After CE, the final separation after common envelope evolution can be estimated by:

$$\frac{a_{\text{final}}}{a_{\text{initial}}} = \frac{M_{\text{core}}M_1}{M_{\text{donor}}} \left(M_1 + \frac{2M_{1,\text{env}}}{\alpha_{\text{CE}}\lambda r_L} \right)^{-1}, \tag{1.50}$$

Where $r_L = (R_{\text{donor}}/a_0)$, is a dimensionless quantity, $M_{1,\text{core}}$ is the core mass of the donor, $M_{1,\text{env}}$ is the envelope mass, and λ is a structure parameter related to the envelope binding energy [19].

An overly efficient common envelope process (high α_{CE}) leads to excessive orbital shrinkage, and has important implications for the merger rate of binary star systems and the detectability

of gravitational wave progenitors [24, 27–29]. This is a known issue in simulations [30], where calibration of α_{CE} is crucial for reproducing observed period distributions of post-CE binaries and for making accurate predictions about gravitational wave progenitors and their underlying populations, including potential AM CVn progenitors.

Angular Momentum Transport and Loss

The prime interest of the AM CVn systems is how such a substantial loss of orbital angular momentum occurs and from what culprits [31]. In the MESA simulation, there are equations for three effects which, coupled, create a substantive loss of angular momentum, decreasing the period and binary separation. The orbital angular momentum of the binary system is[5]

$$J_{orb} = M_1 M_2 \sqrt{\frac{Ga}{M_1 + M_2}}. \tag{1.51}$$

This can be derived from the basic angular momentum formula $J = mvr$ applied to two bodies orbiting their common center of mass, with the reduced mass $\mu = \frac{M_1 M_2}{M_1 + M_2}$ and orbital velocity $v = \sqrt{\frac{G(M_1 + M_2)}{a}}$ [19].

Masses, however, are not constant and can change due to mass transfer such as Roche Lobe Overflow (RLO) as well as due to stellar winds which expel some mass from the convective envelope. The rate of mass loss/mass transfer is given by

$$\dot{M}_1 = \dot{M}_{1,w} + \dot{M}_{RLOF} \quad \text{and} \quad \dot{M}_2 = \dot{M}_{2,w} - f_{mt} \dot{M}_{RLOF}, \tag{1.52}$$

where M_1 is the donor star, $\dot{M}_{1,w}$ is the stellar wind mass loss rate, and $\dot{M}_{RLOF}$ is the mass transfer rate from RLO[16] [5].

To model how the angular momentum equation changes, we need to sum the different angular momentum contributions:

$$\dot{J}_{orb} = \dot{J}_{\text{gr}} + \dot{J}_{ml} + \dot{J}_{mb} + \dot{J}_{ls}, \tag{1.53}$$

---

[16]We will be excluding the f_{mt} term for modelling CO as it refers to the accretion efficiency for which we are not evolving the CO with an accretion disk.

Where $\dot{J}_{gr}$ is the **gravitational radiation** contribution, $\dot{J}_{ml}$ is the **mass loss** contribution, $\dot{J}_{mb}$ is the **magnetic braking** contribution, and $\dot{J}_{ls}$ is the **spin-orbit coupling** contribution [5, 32]. The equation for the total angular momentum loss is implemented in MESA as described in Paxton et al. [5].[17]

Spin-Orbit Coupling and Tides

Spin-orbit coupling effects occur when the spin angular momentum of one or both stars interacts with the orbital angular momentum. This coupling is primarily mediated through tidal interactions, which lead to synchronization, circularization, and alignment of rotation axes in close binary systems [32]. The orbital angular momentum change, Jorb, can be calculated by accounting for total angular momentum conservation while considering losses from other mechanisms and stellar angular momentum loss due to winds. In a fully conservative system, the change in orbital angular momentum equals the negative sum of spin angular momentum changes: $\Delta J_{\text{orb}} = -\delta S_1 - \delta S_2$[18]. This relationship requires correction when mass loss occurs, as winds remove angular momentum from the system. The resulting equation for orbital angular momentum change is:

$$J_{\text{orb}} = \frac{-1}{\delta t}\left(\delta S_1 - S_{1,\text{lost}}\frac{M_{1,\psi}}{M_1} + \delta S_2 - S_{2,\text{lost}}\right). \tag{1.54}$$

$S_{1,\text{lost}}$ and $S_{2,\text{lost}}$ are the spin angular momentum removed from mass loss. The additional factor for the donor accounts for mass lost from the system, excluding mass transfer effects. When mass transfer is absent, this equation simplifies for both stars since $M_{1,\psi}/M_1 = 1$ [5].

Tidal interactions become particularly important in close binaries where at least one component is a giant or a tidally distorted main-sequence star. For LISA gravitational wave progenitors, efficient tidal coupling during the CO stage can significantly affect the final system configuration. The tidal synchronization timescale strongly depends on the ratio of stellar radius to binary separation. [19].

---

[17]The exact formulation of these equations can be found in the MESA instrument papers, particularly Paxton et al. [5], Section 2.3.

[18]The δ here refers to a time-step as these are equations for the MESA code. The timestep is the optimized simulation time unit.

Gravitational Wave Radiation

The angular momentum loss from gravitational waves is

$$\dot{J}_{gr} = -\frac{32}{5c^5}\left(\frac{2\pi G}{P_{orb}}\right)^{7/3}\frac{(M_1 M_2)^2}{(M_1 + M_2)^{2/3}} \tag{1.55}$$

This expression follows from Einstein's quadrupole formula for gravitational radiation, where the rate of energy loss is proportional to the third time derivative of the quadrupole moment squared, translated to angular momentum.

This mechanism dominates for systems with periods less than approximately 2 hours and is particularly important for AM CVn systems, which emit gravitational waves in the mHz frequency range detectable by future space-based detectors like LISA [33, 34]. For AM CVn binaries with periods of 5-65 minutes, gravitational wave radiation becomes the primary driver of orbital evolution [31].

Mass loss and Stellar Winds

Stellar winds expel mass that contains the specific angular momentum of its host star. The angular momentum loss rate due to stellar winds can be expressed as [7]:

$$\dot{J}_m = \left[\left(\dot{M}_{1,w} + \alpha_m \dot{M}_{RLOF}\right)M_1^2 + \left(\dot{M}_{2,w} + \beta_m \dot{M}_{RLOF}\right)M_2^2\right]\frac{a^2}{(M_1 + M_2)^2}\frac{2\pi}{P_{orb}}$$
$$+ \gamma_m \dot{\delta}_m \dot{M}_{RLOF}\sqrt{G(M_1 + M_2)a}, \tag{1.56}$$

where α_{mt}, β_{mt}, and δ_{mt} represent the fractions of mass transferred that is lost from different areas of the system. For low-mass stars relevant to AM CVn progenitors, wind mass loss rates are usually low during the main sequence, but increase substantially during the red giant phase [19].

Magnetic Braking

Magnetic braking occurs when ionized stellar wind particles follow magnetic field lines extending from a star's surface, effectively acting as extended lever arms that extract angular momentum [35].

Figure 1.9: Schematic of an ionized gas particle extending from the surface of a star, creating the *magnetic braking* effect.

For a magnetically active star with a convective envelope and when there is a tidally coupled orbit, the angular momentum loss rate can be approximated as:

$$\dot{J} = -3.8 \times 10^{-30} M R_\odot^4 \left(\frac{R}{R_\odot} \right)^{\gamma_{mb}} \Omega^3, \tag{1.57}$$

where γ_{mb} is a free parameter[19] which affects the torque based on distance from the stellar center, and Ω is the stellar surface rotation rate.

AM Canum Venaticorum

AM CVn systems are ultra-compact binaries consisting of a carbon-oxygen white dwarf accreting from a helium-rich donor. Their formation requires significant orbital angular momentum loss to achieve their characteristic short periods (5-65 minutes) [31]. These close binary systems emit gravitational waves at the mHz frequency and are thus a source of interest for future space-based gravitational wave detectors such as the Laser Interferometer Space Antenna (LISA) [33, 34, 36].

Multiple formation channels are possible [31]:

---

[19]This parameter is set to 3 in the default `MESA` code.

- White dwarf channel: A double white dwarf system that evolves to shorter periods via gravitational wave radiation until mass transfer begins

- Helium star channel: A white dwarf accreting from a helium star donor that gradually loses mass and becomes semi-degenerate

- Evolved CV channel: An evolved main sequence donor that has lost its hydrogen envelope, leaving a helium-rich core

Understanding which channel dominates requires accurate modeling of the processes described above, particularly common envelope evolution and magnetic braking in low-mass stars. The period distribution and donor mass range of observed AM CVn systems provide important constraints on these evolutionary processes and their parameterizations [37].

Recent population synthesis studies suggest that the Galaxy may harbor approximately 112,000 helium-donor AM CVn stars with orbital periods less than 42-43 minutes, of which about 500 may be detectable by LISA with a signal-to-noise ratio greater than 5 during a 4-year mission [38]. However, the actual space density of these systems remains uncertain, with observational constraints from systematic searches suggesting lower numbers than predicted by theory [39].

The thermal state of the accreting white dwarf in AM CVn binaries is also of interest, as it contributes significantly to their optical and ultraviolet emission. For systems with orbital periods longer than 40 minutes, the white dwarf's effective temperature is set by its cooling as the mass transfer rate decreases dramatically [40]. Understanding this evolution is crucial for interpreting observations and for developing targeted searches for these elusive systems.
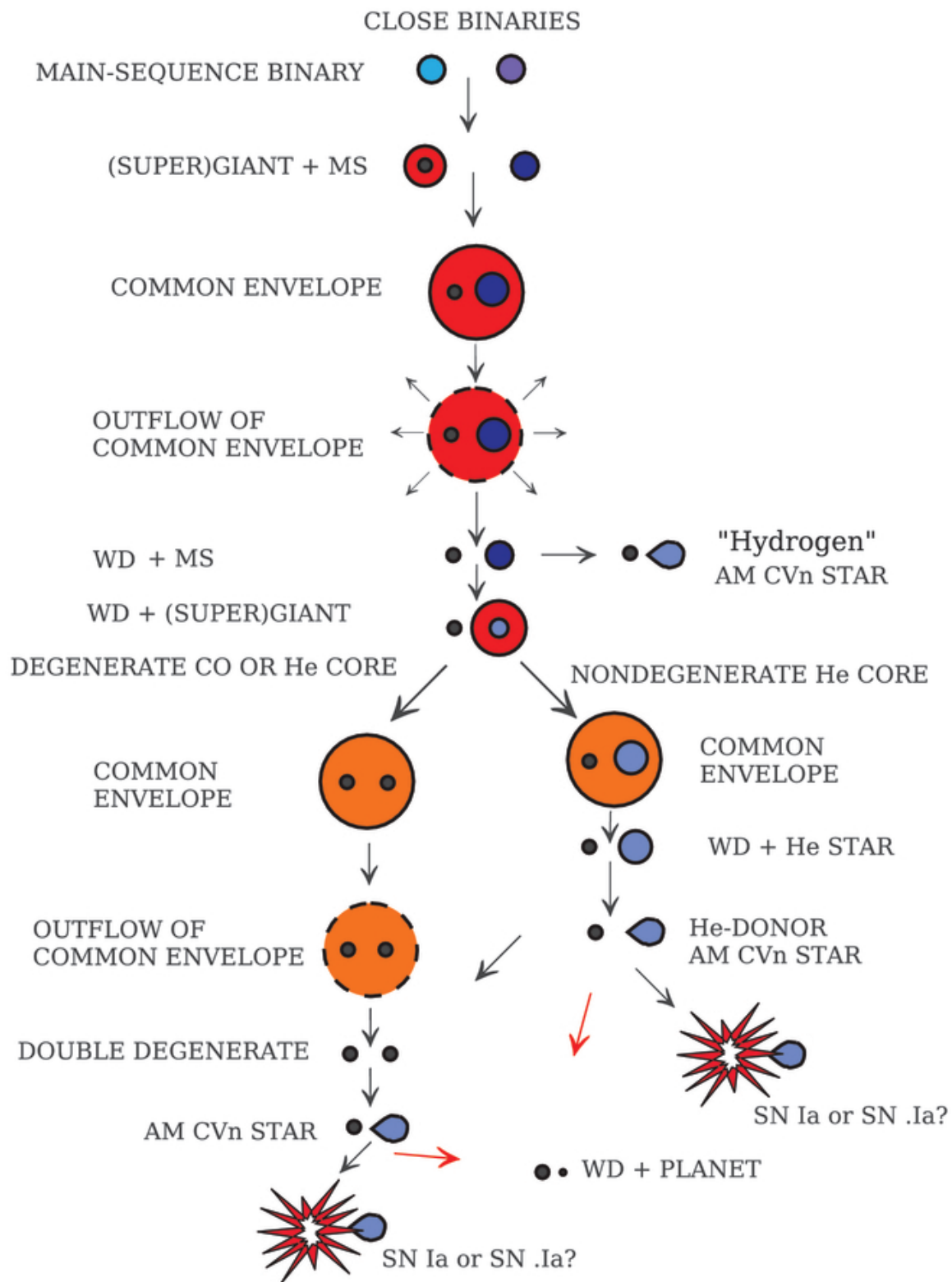
Figure 1.10: AM CVn formation channels van den Heuvel Diagram. Adapted from [31].

C h a p t e r 2

SIMULATIONS: MESA AND POSYDON

Until the advent of *simulations*, Astronomy was limited to the *theory* and *observation*. It is clear that in the landscape of astrophysical research, the cyclical combination of these three concepts forms the foundation of this thesis. We use both the **M**odules for **E**xperiments in **S**tellar **A**strophysics (MESA) and a **PO**pulation **SY**nthesis with **D**etailed binary-evolution simulati**ON**s (POSYDON) in which we vary initial conditions such as mass, period, and mass ratio, and determine the effect on the evolution of stars.

2.1   Detailed Stellar Evolution Models

There have been computations that attempt to simulate the evolution of stars since the early 70s with the STARS code [41]. Many stellar model-building simulations have been created, however, none are as self-consistent and widely used as MESA [4]. MESA is open source, which renders it, by far, the most up-to-date stellar astrophysics code; currently named in the *Astro 2020 Decadal Survey* [42] as one of the leading methods for studying stellar evolution. The code, written in FORTRAN, solves the stellar structure equations and is easily able to, at the minimum, evolve a star from ZAMS to the WD cooling track. It can handle challenging phases like helium core flash and thermal pulses. It solves the coupled structure equations using a Newton-Raphson method with analytic Jacobians. MESA also supports binary stellar evolution, making it an ideal code to build our stellar models. The code mainly solves the differential equations (mass conservation, momentum conservation, energy conservation, composition evolution) through time. I list them here again for convenience:

$$
\begin{cases}
\frac{\partial m}{\partial r} = 4\pi r^2 \rho \\[2mm]
\frac{\partial P}{\partial r} = -\frac{Gm\rho}{r^2} \\[2mm]
\frac{\partial L}{\partial r} = 4\pi r^2 \rho \varepsilon \\[2mm]
\frac{\partial T}{\partial r} = -\frac{3\rho\kappa L}{16\pi acT^3 r^2}
\end{cases}
$$

`MESA` maintains the underlying assumption that a star is spherically symmetric and is in hydrostatic equilibrium. `MESA` divides the stellar structure into hundreds or thousands of concentric shells. Each cell contains information on both the mass-averaged variables such as density, temperature, and composition, as well as shell boundary variables such as mass, radius, luminosity, and velocity. `MESA` adjusts the thickness of these shells to maintain resolution and accuracy when variables change rapidly (such as at convective boundaries or in nuclear-burning shells).
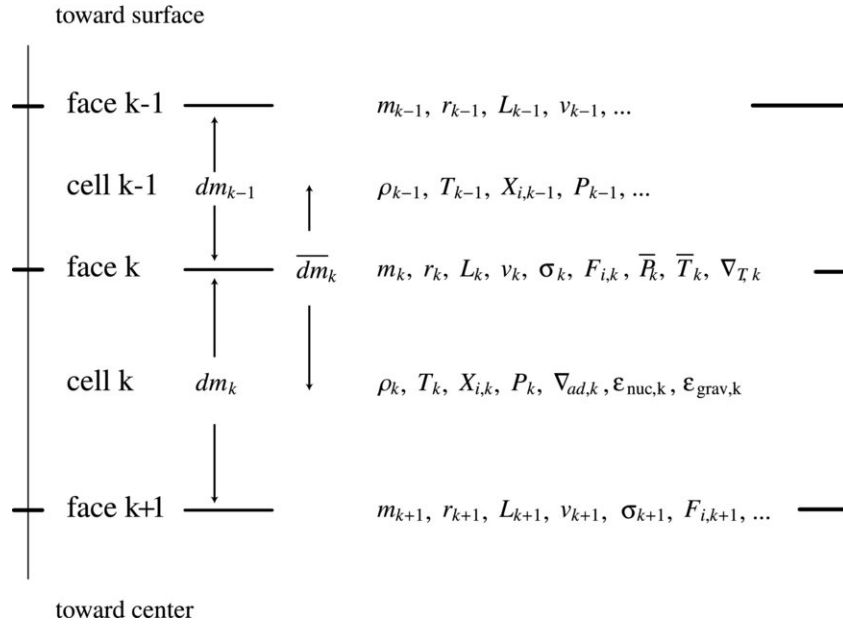
toward surface

face k-1 $m_{k-1},\ r_{k-1},\ L_{k-1},\ v_{k-1},\ ...$

cell k-1 dm_{k-1} $\rho_{k-1},\ T_{k-1},\ X_{i,k-1},\ P_{k-1},\ ...$

face k $\overline{dm_k}$ $m_k,\ r_k,\ L_k,\ v_k,\ \sigma_k,\ F_{i,k},\ \overline{P}_k,\ \overline{T}_k,\ \nabla_{T,k}$

cell k dm_k $\rho_k,\ T_k,\ X_{i,k},\ P_k,\ \nabla_{ad,k},\ \varepsilon_{\text{nuc,k}},\ \varepsilon_{\text{grav,k}}$

face k+1 $m_{k+1},\ r_{k+1},\ L_{k+1},\ v_{k+1},\ \sigma_{k+1},\ F_{i,k+1},\ ...$

toward center

Figure 2.1: A schematic [4] depicting the shell (cell) configuration of `MESA`.

Moreover, `MESA` has the capability of binary stellar evolution. It accurately handles important processes such as RLOF, mass accretion, and stellar wind mass loss. It accounts for changes in orbital angular momentum due to gravitational wave radiation, magnetic braking, and spin-orbit coupling. Additionally, `MESA` also incorporates thermohaline mixing as well as the effects of stellar rotations. `MESA` evolves a system of binary stars through their MS as well as PMS and CO evolution.

For detached, single-star evolution, we feed `MESA` a set of uniformly distributed initial stellar masses at solar metallically and obtain the evolutionary track for HMS and HeMS stars. The full single-star evolution is important for our study of binary stellar evolution as

allows us to scrutinize simulation parameters to have confidence in the detached evolution (i.e single star evolution) before running thousands of binary evolution simulations.

Table 2.1: Summary of the Five Detailed Single- and Binary-star Model Grids

Initial State		Parameters' Range and Resolution								
Star 1	Star 2	M_1 [$M_\odot$]	$\Delta \log_{10} M_1$	M_2^{a} [$M_\odot$]	$\Delta \log_{10} M_2$	q	Δq	P_{orb} [day]	$\Delta \log_{10} P_{\mathrm{orb}}$	N^{b}	Failures$^{\mathrm{c}}$
ZAMS	...	0.5–10	0.014	...	...	...	...	...	...	97	0%
ZAHeMS$^{\mathrm{d}}$	...	0.1–12	0.055	...	...	...	...	...	...	99	0%
ZAMS	ZAMS	0.8–80	0.025	...	...	0.1–1	0.1 dex	0.2 − 1000	...	1447	8.5%
Evolved, H-rich$^{\mathrm{e}}$	CO	0.1–12	0.06	1–35.88	0.074	...	...	0.01 - 1000	...	2024	1.6%
ZAHeMS	CO	0.1–12	0.055	1–35.88	0.074	...	...	0.01 - 1000	10	2022	0.1%

Notes.
$^{\mathrm{a}}$ We exclude secondary masses less massive than 0.1 Msol. $^{\mathrm{b}}$ Total number of models in this grid.
$^{\mathrm{c}}$ Percentage of models that stopped due to numerical convergence errors before reaching one of our stopping conditions.
$^{\mathrm{d}}$ Zero-age He main sequence stars.
$^{\mathrm{e}}$ Although this grid is initialized with H-rich stars at ZAMS, we ignore the portion of each simulated binary's evolution before the onset of RLO. The initial state of Star 1 in this grid is therefore somewhat arbitrary.

For binary evolution, we are concerned with the coupled evolution of the two stars. We create a binary stellar evolution **grid**[1] of Hydrogen Main Sequence stars (HMS-HMS), as well as Compact Object and Hydrogen Main Sequence (CO-HMS) and Compact Object and Helium Main Sequence (CO-HeMS) evolution. We initialize new binary MESA simulations with ranges for mass ratio q, orbital period (in days) P_{orb}. We are running our simulations specifically at solar metallicity (Z=0.0142 dex). We take the donor star to be star 1. We want to constrain our experiment to the formation of White Dwarf stars, so we are choosing an initial mass of M_1 as being lower than solar mass $\approx 0.8 M_\odot$[2] up to 8 $M_\odot$ s. We run 1000 binary star simulations spread over 10 different values of q, logarithmically spaced between 0.1 and 0.99, totaling $\sim$ 1000 binaries per grid[3]. Our total amount of simulations is $N = 5689$. MESA will evolve these binaries until they terminate at unstable mass transfer (MT) stages such as unstable RLO, ultimately leading to CE evolution. MESA is not capable of fully modeling RLO and CE as the CE stage is highly non-equilibrium and necessarily 3D with rapid mass loss; MESA cannot capture the entire hydrodynamic and thermodynamic complexities of this phase. Moreover, to conduct a large study of the population of AM

---

[1]A grid denotes a slice of the parameter space of orbital period versus donor mass for a single mass ratio.
[2]It is well known that for stars initially above $8 M_\odot$, a star can begin to show signs of supernova and a subsequent neutron star or black hole stage
[3]We go back and add to any empty sections of the parameter space with an extension of the grid. This is why we see more than 1000 models per grid in Table 2.1.

CVn's, we would need a way to produce these binary systems rapidly. Although many of our models break symmetry, we are still able to use `MESA`, as for most of our stars' lifetime, they follow our basic assumptions. As long as we pay close attention to the termination conditions, we can understand what happens between our `MESA` models. To continue, we utilize another code, `POSYDON`, that can fill in the gaps between our `MESA` grids by calculating through asymmetric evolutionary stages and generating large-scale populations for our study of AM CVn's in the Milky Way.

2.2 Binary Population Synthesis

Creating a large-scale population of binary stars with a full evolutionary history, via numerical calculation alone, would be a feat. To understand the population of a stellar object that is known to be a product of binary interactions, we need to be able to model all the possible formation channels that could form objects in that population. Codes such as `MESA` can evolve each binary through binary interactions, but to calculate the evolution of each binary in a minimally realistic galactic population of binaries, $N = 10^6$, you would need more than one month of a 10,000 core HPC facility [19]. A solution to this is *Fast Binary Population Synthesis*. This method relies on a library of pre-calculated grids to interpolate and the ability to do on-the-fly calculations through certain evolutionary stages. One code that successfully uses this method is `POSYDON` [30]. `POSYDON` is built upon a detailed grid of stellar evolution models created using `MESA`. `POSYDON` creates a population of binaries by randomly sampling initial parameters such as the masses of the two stars and their orbital period from user-defined or standard distributions like initial mass functions (IMFs) and orbital period distributions. Different star-formation rates (SFRs) can be modeled by modifying the distribution of birth times. `POSYDON` offers two options: a burst of star formation (all binaries have identical birth times) or a constant SFR (birth times are randomly generated from a uniform distribution within a user-defined range). [30]. The initial binaries are set at the zero-age main sequence (ZAMS). In the evolution phase, these initially generated binaries evolve over time using detailed stellar structure and binary evolution models.`POSYDON` uses pre-calculated grids of these models and on-the-fly

calculations for certain evolutionary phases like common envelope (CE) evolution and core collapse.
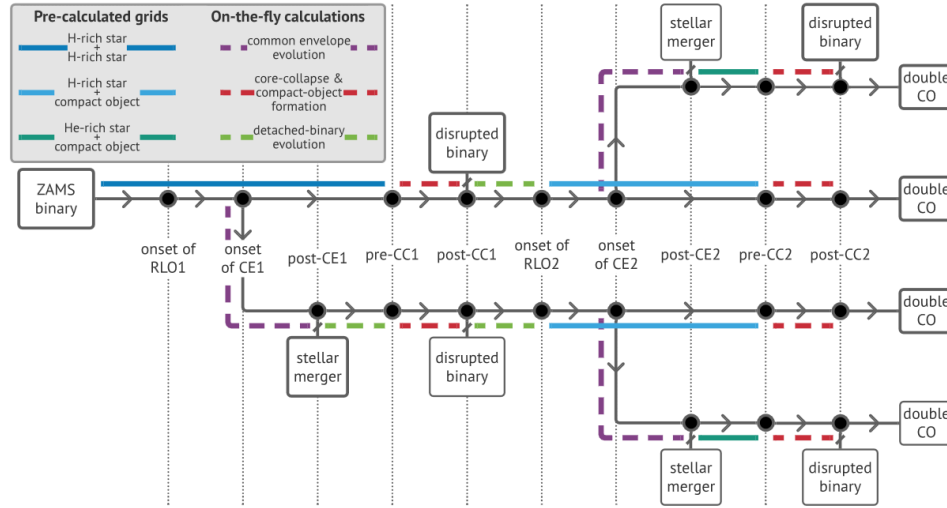

Figure 2.2: A schematic of the structure of POSYDON. The dotted lines are calculations made on-the-fly while the filled lines are the various detailed grids that POSYDON works between [30].

POSYDON employs a specific interpolation scheme to estimate the evolutionary paths and final properties of binary star systems for which detailed MESA simulations on its pre-calculated grids do not exist. The interpolation scheme in POSYDON fundamentally relies on an N-dimensional linear interpolation. The accuracy of the interpolation scheme is evaluated using validation data sets, which consist of binary systems whose detailed evolution was simulated but not used in training the classifier or the interpolator. Errors in POSYDON's interpolated parameters are typically around 1% or lower.

Ultimately, this process of sampling from the detailed grid, calculating through dynamic evolutionary scales, and interpolating points within the grid continues until each binary reaches a final state, such as a double compact object, a merger, or disruption. The resulting population of evolved binaries can then be used for comparison with astronomical observations.
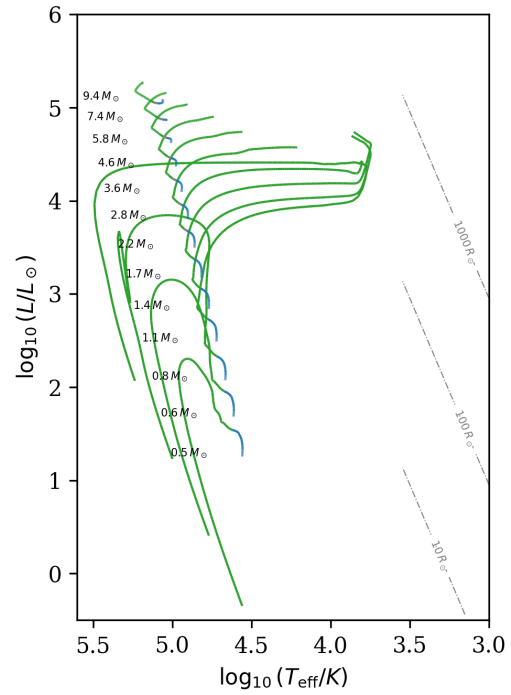
Chapter 3

RESULTS AND ANALYSIS

3.1 Grid Analysis

Single Star Evolution
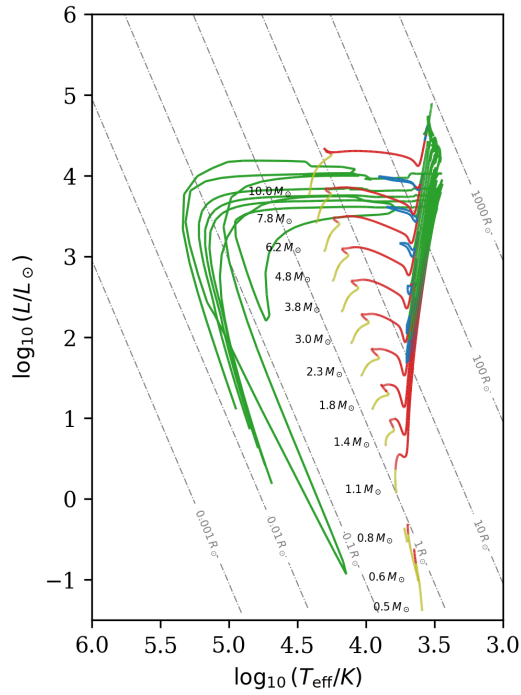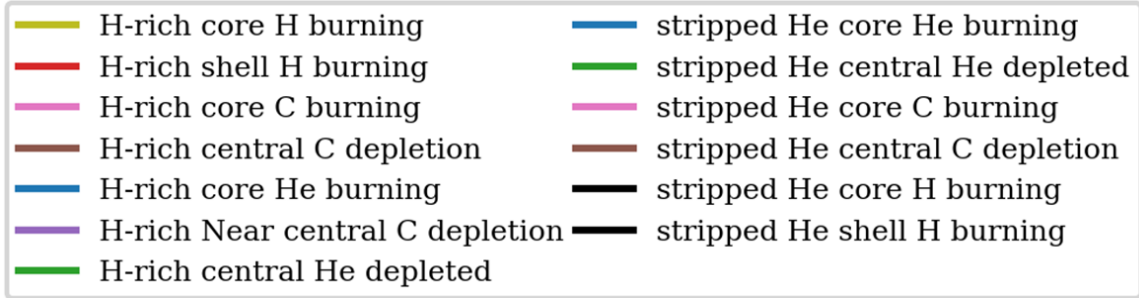
(a) Single star Hydrogen Main Sequence evolutionary tracks.

(b) Single star Helium Main Sequence evolutionary tracks.

Figure 3.1: Evolutionary tracks for stars of different masses on the HR diagram. Panels separate hydrogen (left) and helium (right) burning stars of various masses (in $M_\odot$), plotted as luminosity versus effective temperature.

The figures above describe the detached, single-star evolution of initial masses with a detailed overview of the stages of nuclear burning. We see that our systems reach the end of their life as WD stars after going through the WD cooling track. We can observe that the stars begin on the main sequence and after exhausting their core hydrogen, they become cooler. They climb upward, becoming more luminous, as they enter the red giant phase. Ultimately, they find themselves as WD compact object remnants.
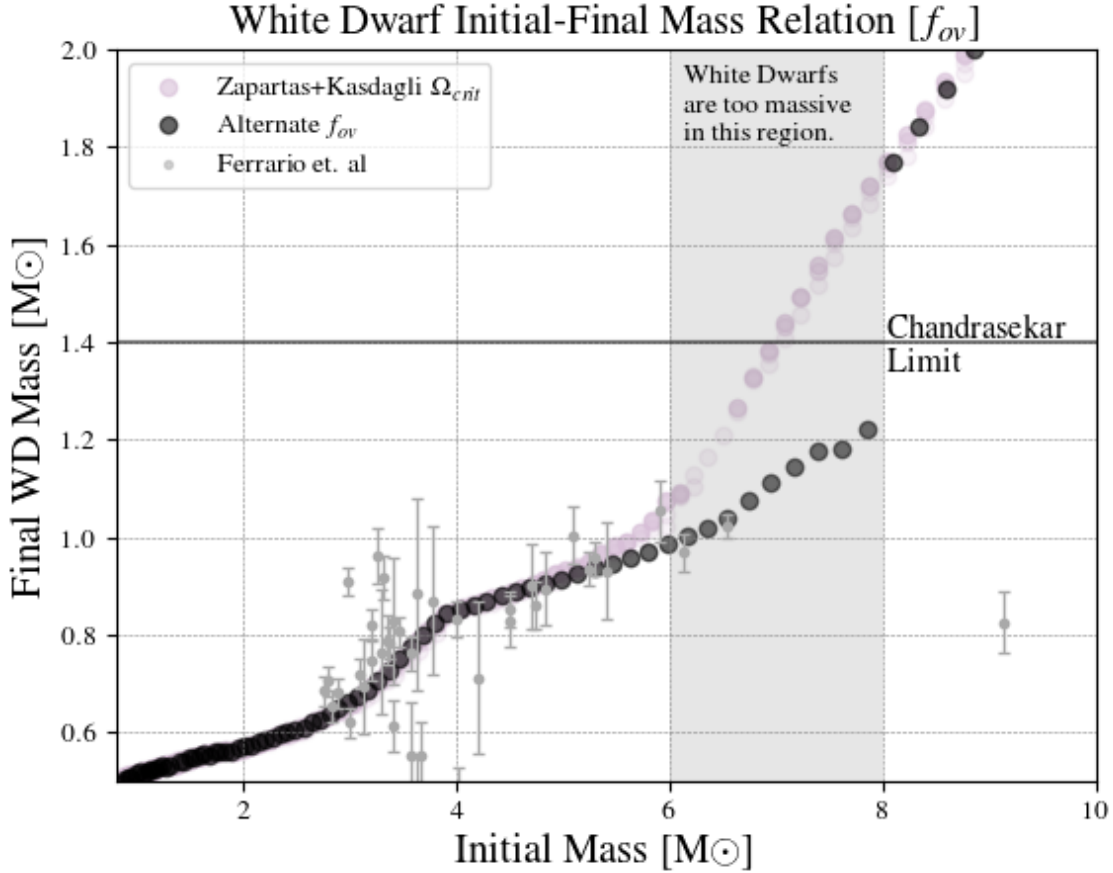

Figure 3.2: Observationally constrained Initial-Final Mass Relation with $f_{ov} = 1.6 \times 10^{-2}$ for initial mass $< 8M_\odot$ and $f_{ov} = 4.15 \times 10^{-2}$ for initial mass $> 8M_\odot$. Observations of WD final masses and predicted initial masses are yielded from 8 open clusters.

In improving the accuracy of our simulation, we focused on obtaining a more observationally consistent initial-final mass relation (IFMR) for WD stars. We were influenced to take this step after noticing that our Initial Final Mass Relation (IFMR) produced WD's that were too massive in the 6-8 initial $M_\odot$ range [43]. Our IFMR was not consistent, in that range, with MIST isochrones and observed open cluster data [44]. In order to constrain the final

White Dwarf mass, we introduced a step function for the convective overshoot parameter f_{ov} in the exponential term of the default convective boundary mixing (CBM) prescription in `MESA`,

$$D_{CBM}(r) = D_0 e^{\frac{-2(r-r_0)}{f_{ov}H_{p,0}}} \tag{3.1}$$

where the $r-r_0$ is the size of the mixing boundary, and $H_{p,0}$ is the pressure scale height. D_0 is the convective mixing efficiency for $r = r_0$ [45]. We used a value of $f_{ov} = 1.6 \times 10^{-2}$ for initial mass $< 8M_\odot$ and $f_{ov} = 4.15 \times 10^{-2}$ for initial mass $> 8M_\odot$. The overshoot parameter constrains the mixing of material between convective boundaries. This material from outside the core mixes with the core and increases the final core remnant mass. We plotted data (Zapartas+Kasdagli) of single-star HMS grids which had varying critical rotation (Ω_{crit}) values alongside our new f_{ov} prescription. Moreover, to be more succinct in comparison with similar studies, we plotted the observational data of WD initial and final masses from [46] as constraints on how physically plausible our results were. It is important to note, the observational constraints come with their uncertainties; this prescription, however, is necessarily ad-hoc as convective overshoot is not a well-understood phenomenon, which requires further analysis.

Hydrogen Main Sequence and Hydrogen Main Sequence

For binary stellar evolution grids, we will look mainly at the He-star formation[1]

---

[1] It is important to note that the following section on the analysis of the population came first, and then a deeper analysis was conducted on the grids. As we will discuss in the next section, the He star channel is the most probable formation channel for the AM CVn.
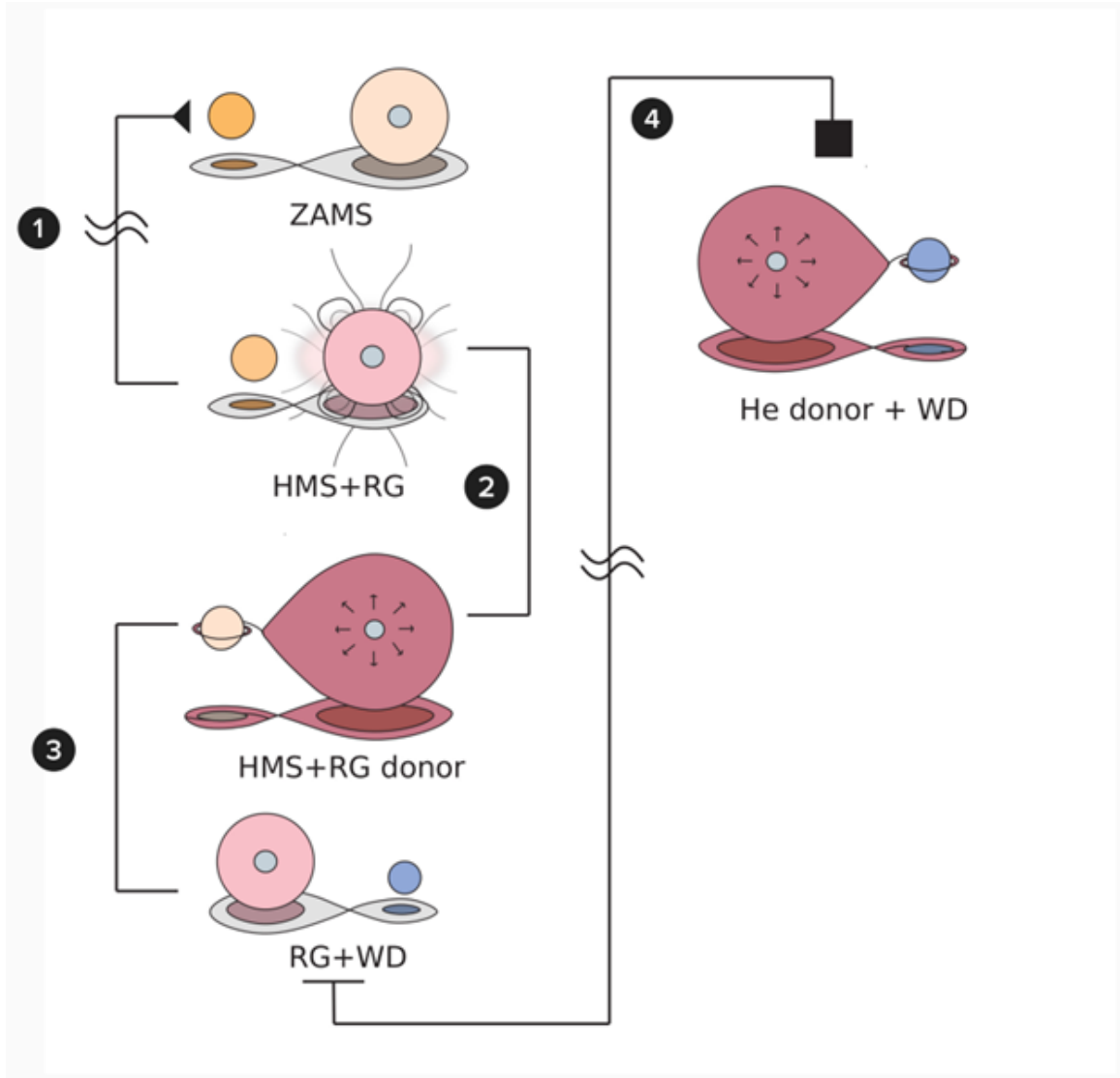
Figure 3.3: Helium Star Channel Evolution van den Heuvel Diagram. The ≈ symbol denotes a long timescale.

Our approach is to classify important dynamic stellar evolution stages where MESA fails and classify them with the use of POSYDON. Figure 3.5 shows a set of distributions of termination conditions across our grid, focusing on systems experiencing stable or unstable RLO. In our HMS-HMS grid, we are looking mainly at the beginning of the helium star donor channel. The beginning of the formation of an AM CVn is often categorized as an instance of unstable MT during a convective star, ultimately leading to a common envelope. This is a key factor of the necessary orbital shrinkage that brings the two stars to such a short period. Take, for instance, a binary system[2]. The termination is ultimately due to the

---

[2]Horizontal axes are reversed on the H-R diagram

onset of CE (top right). with an initial M_{donor} of $6.19 M_\odot$, P_{orb} of 200.27 days, and a mass ratio $q = 0.29$.
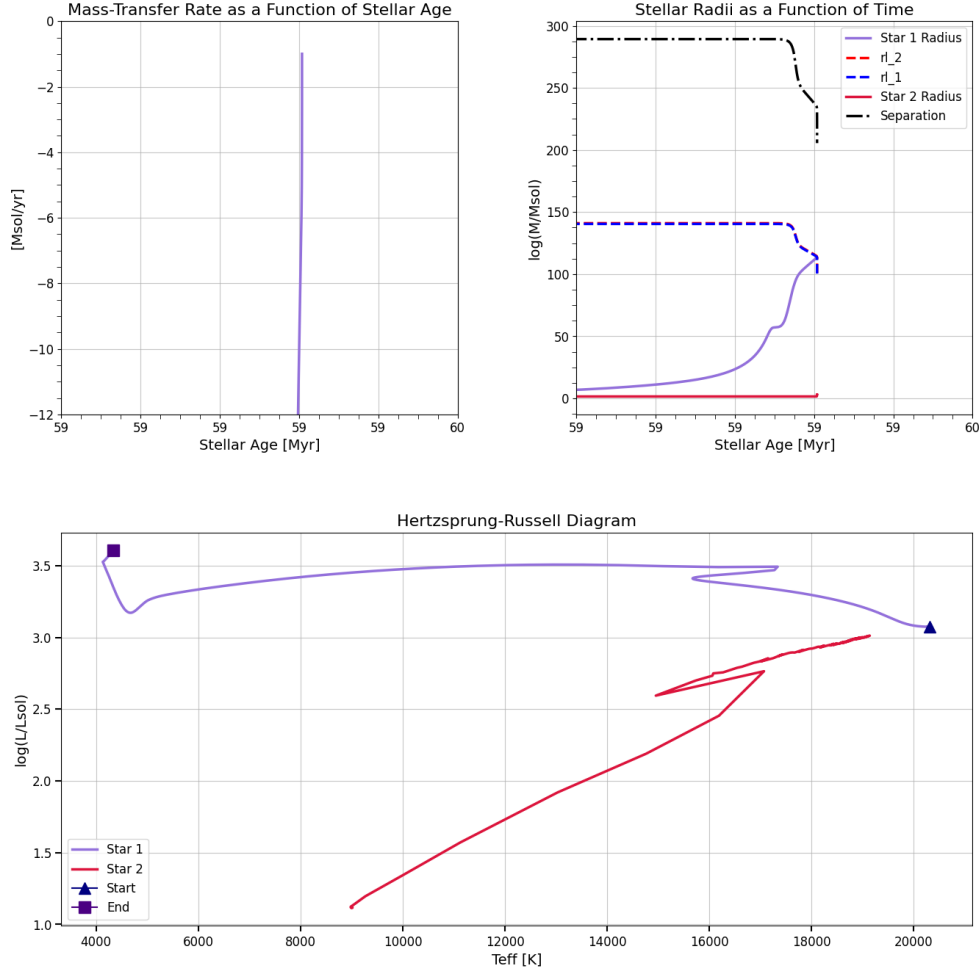

Figure 3.4: A `MESA` model with initial parameters $M_{\mathrm{donor}} = 6.19 M_\odot$, $P_{\mathrm{orb}} = 200.27$days, and a mass ratio $q = 0.29$ undergoes unstable MT during the red-giant phase (bottom)

We find that the system undergoes a runaway MT that ultimately leads to the termination of the simulation. By plotting the Roche-lobe radius 1 and 2 using

$$r_{\ell 2} = (-0.785 q^{10.5} e^{-0.188 q} + 1.004) r_{\ell 1}, \tag{3.2}$$

We can deduce that the radius of the donor star exceeds $r_{\ell 2}$. This is the onset of CE, and for MESA, it increases the resolution of the time steps to attempt to model the system, but ultimately fails due to a high level of asymmetry. For 10 different values of q, we found a strong correlation between lower values of q and higher rates of unstable MT. For $q = 0.2$ we found the highest probability of unstable MT. The high probability of runaway MT

cases per lower mass ratio directly agrees with [20–22]. Moreover, as described in [19], the orbital period shrinks greatly during the post-CE1 stage, in line with early stages in the He-star channel [31]. We find, however, that for the CO HMS grid, our mass transfer cases are split rather similarly among high and low mass ratios, with the least common being $0.3 \leq q \leq 0.5$. In the CO HMS grid, a system is more likely to have unstable mass transfer at lower mass ratios and have stable mass transfer at higher mass ratios.

(a)

(b)

(c)

(d)

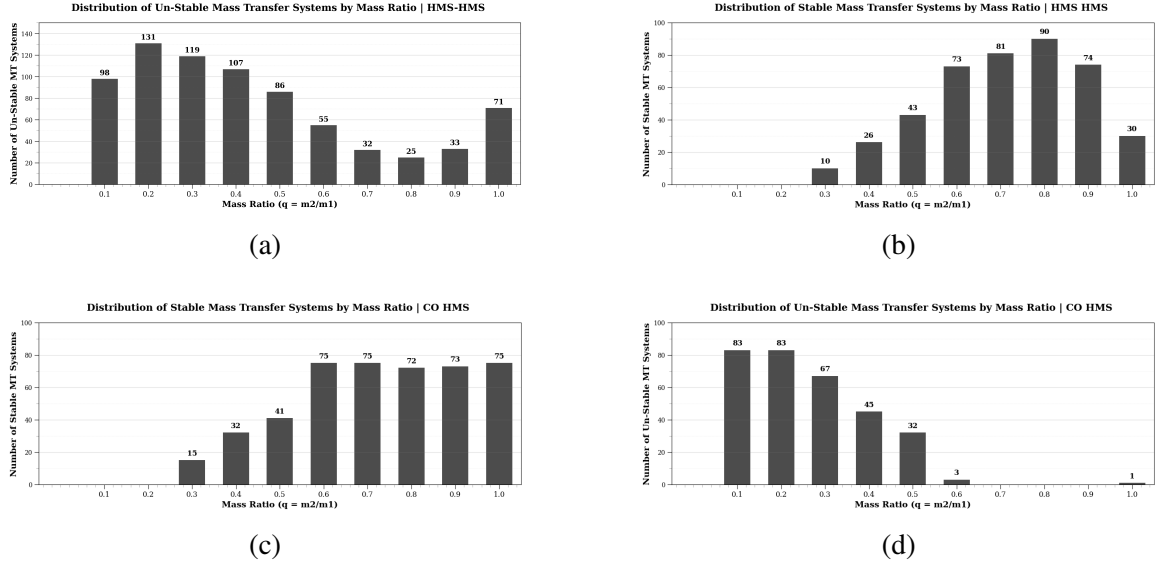Figure 3.5: The frequency of Mass Transfer Systems for mass ratio $0.1 < q < 1.0$: (a) unstable mass transfer systems for the HMS HMS grid, (b) stable mass transfer systems for the HMS HMS grid, (c) stable mass transfer systems for the CO HMS grid, and (d) Unstable Mass transfer systems for the CO HMS grid.

Figure 3.6: Slices of the binary-star model **grids** are shown for a range of mass ratios $0.1 < q < 1$ with both stars starting as H-rich ZAMS stars. The Symbols summarize each model's outcome: squares mark systems that underwent stable or no mass transfer and evolved to the end of one star's life, while diamonds indicate systems halted unstable mass transfer. red x's highlight cases that stopped early for numerical reasons.
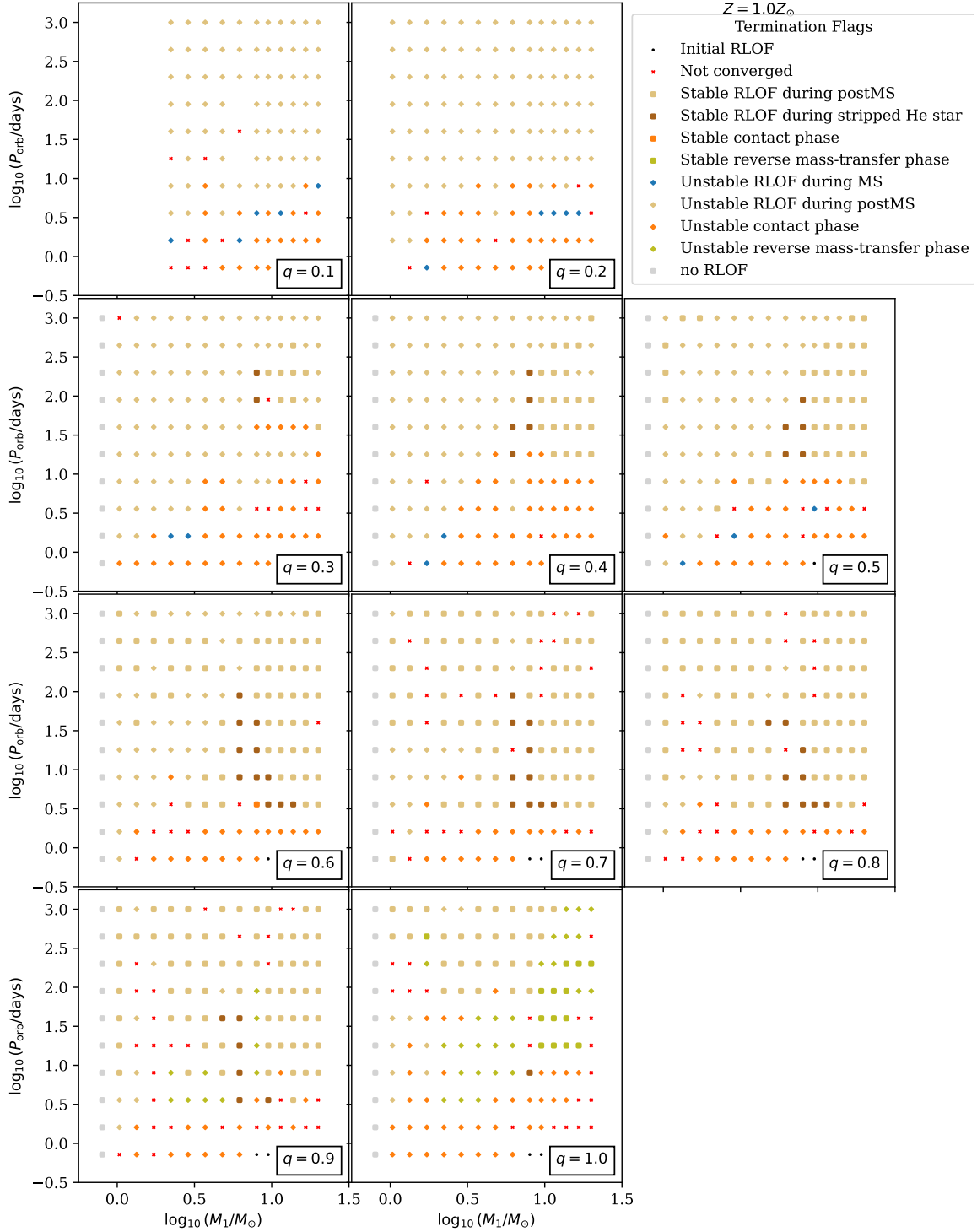
Figure 3.7: Slices of the binary-star model **grids** are shown for a range of mass ratios 0.1 < q < 1 with the donor star starting as a H-rich ZAMS star and the other a Compact Object. The Symbols summarize each model's outcome: squares mark systems that underwent stable or no mass transfer and evolved to the end of one star's life, while diamonds indicate systems halted unstable mass transfer. Red x's highlight cases that stopped early for numerical reasons.
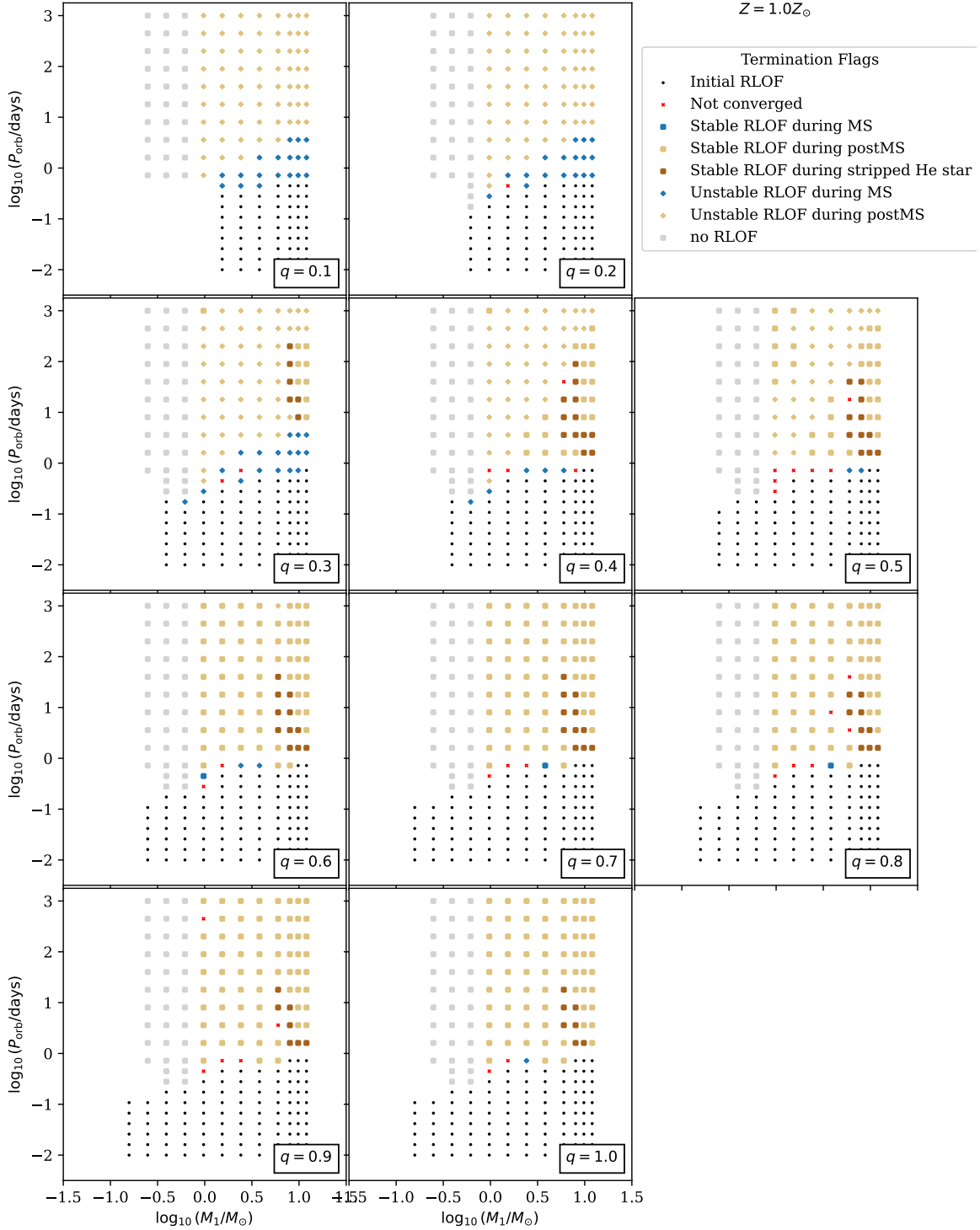
Helium Main Sequence and Compact Object

The Compact Object and Helium Main Sequence grids are characterized by a point mass compact object and a helium-burning main sequence star. It is in this grid where we find a set of models that represents AM CVn-like systems. looking at mass transfer cases across the grid, we find that most unstable mass transfer occurs immediately at $q < 0.2$, yet for stable mass transfer cases, we find that they are frequent from $0.4 < q < 1.0$. We can begin our classification for systems that survive this grid and have stable mass transfer, as they might be an AM CVn if their orbital period drops below 1 hour. In Figure 3.9, we have plotted a distribution of our AM CVn population obtained from our grid. Our classification scheme is far from rigorous, as it only accounts for systems with orbital periods less than 60 minutes undergoing mass transfer. The snapshot taking is at the end of the life of the system, so many of these models have perhaps merged. Thus, a representation of the time evolution of our grids (Figure 3.10) reveals a more accurate representation of the AM CVn subpopulation as the orbital period changes drastically during mass transfer. Systems below 5 minutes are essentially merged systems.

Distribution of Un-Stable Mass Transfer Systems by Mass Ratio | CO HeMS

(a)

Distribution of Stable Mass Transfer Systems by Mass Ratio | CO HeMS
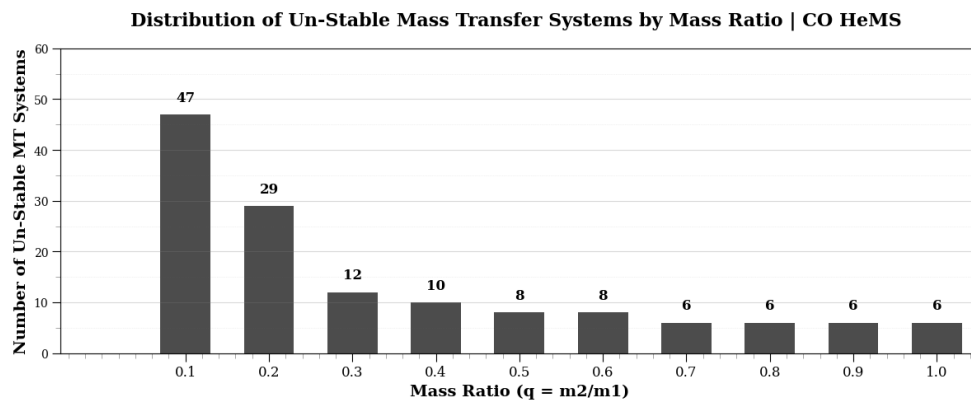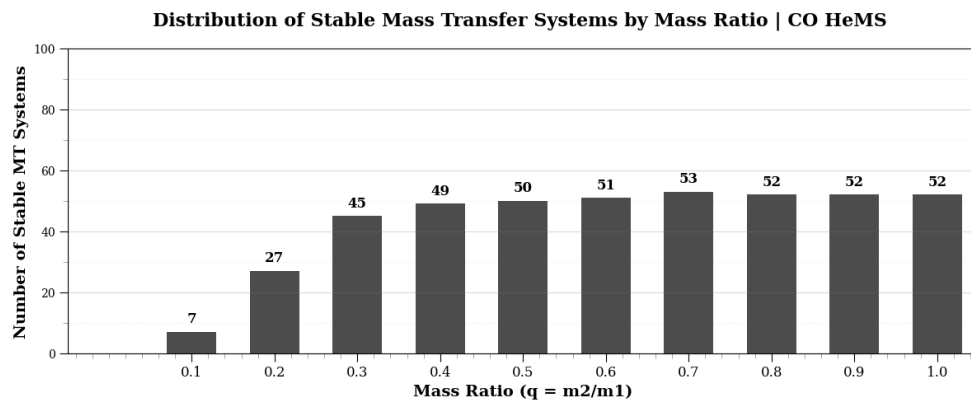
(b)

Figure 3.8: Two plots showing mass transfer frequency for a CO He MS grid: (a) unstable mass transfer systems, and (b) stable mass transfer systems.
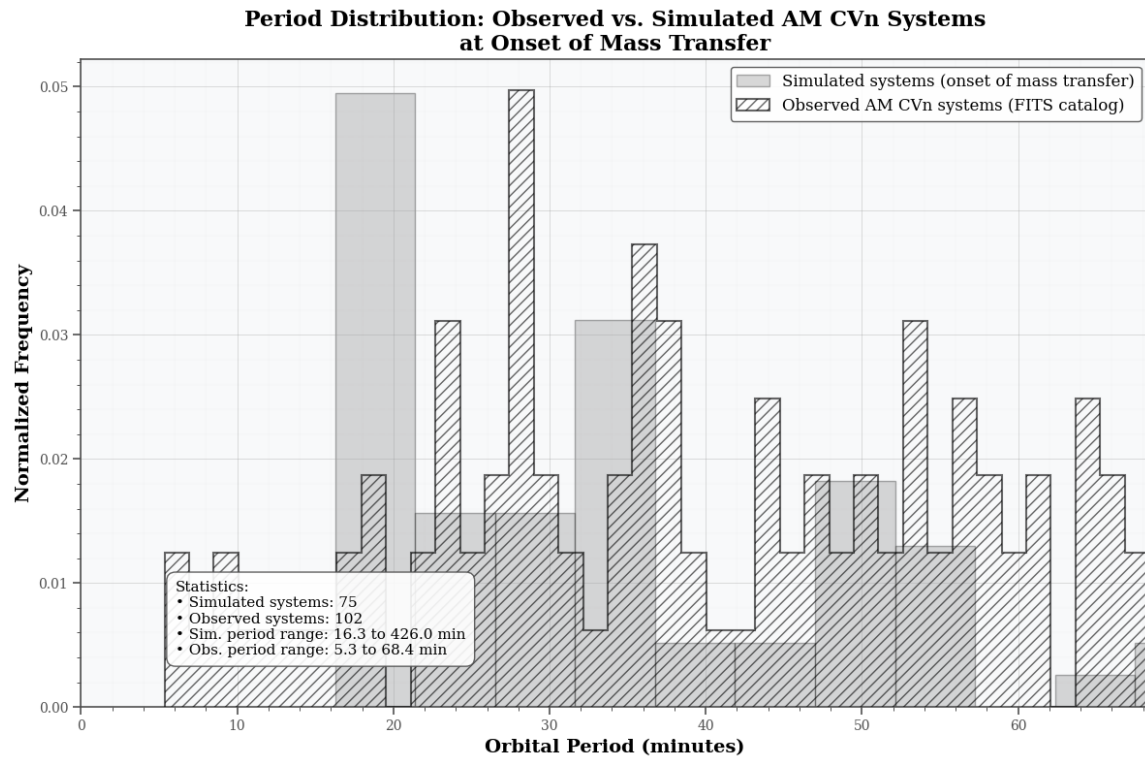
Figure 3.9: Distribution of orbital periods from simulated systems at the onset of RLO2 with Observational Catalogue Data [47].
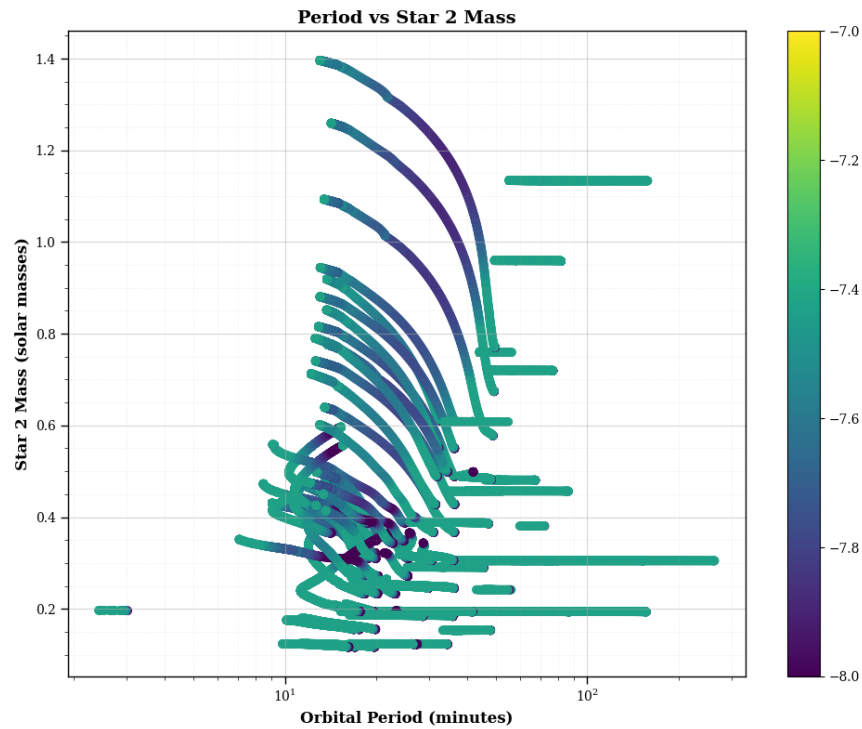
Figure 3.10: AM CVn time evolution beginning with the moment the outer envelope passes the Roche-lobe initiating mass transfer.
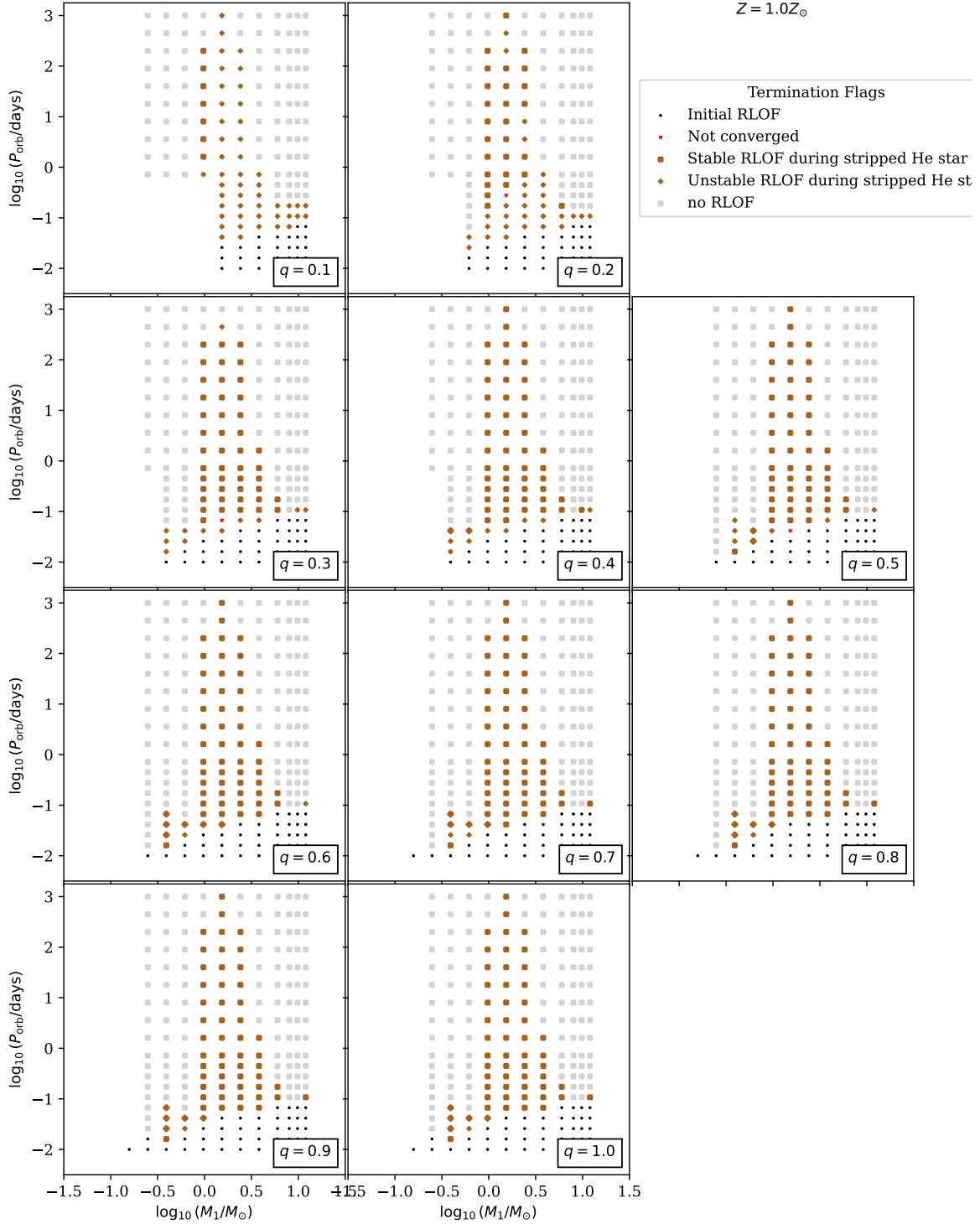
Figure 3.11: Slices of the binary-star model **grids** are shown for a range of mass ratios $0.1 < q < 1$ with the donor star starting as He-rich ZAMS star and the other a Compact Object. The Symbols summarize each model's outcome: squares mark systems that underwent stable or no mass transfer and evolved to the end of one star's life, while diamonds indicate systems halted unstable mass transfer. Red x's highlight cases that stopped early for numerical reasons.
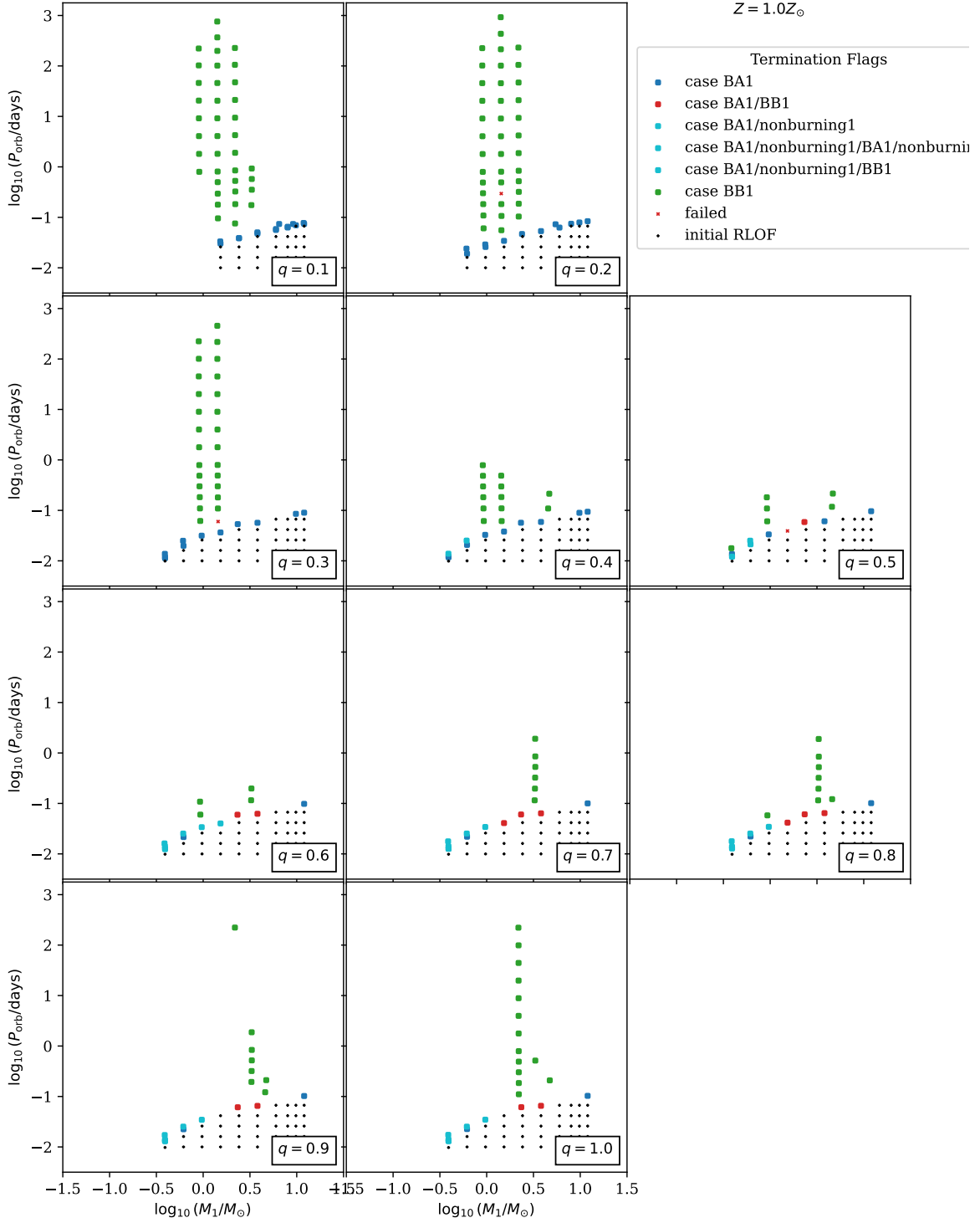
Figure 3.12: Slices of the binary-star model **grids** are shown for a range of mass ratios $0.1 < q < 1$ with the donor star starting as He-rich ZAMS star and the other a Compact Object. The symbols summarize each model's mass transfer type. Red x's highlight cases that stopped early for numerical reasons.

Discussion

3.2 Population Analysis

Our resulting population of 10^6 low-mass to intermediate-mass binary stars.

Table 3.1: Population Output Metallicity and Mass Data

| metallicity $[Z_\odot]$	simulated_mass $[M_\odot]$	underlying_mass $[M_\odot]$	N
1.0	2.53476×10^6	6.81751×10^6	10^6
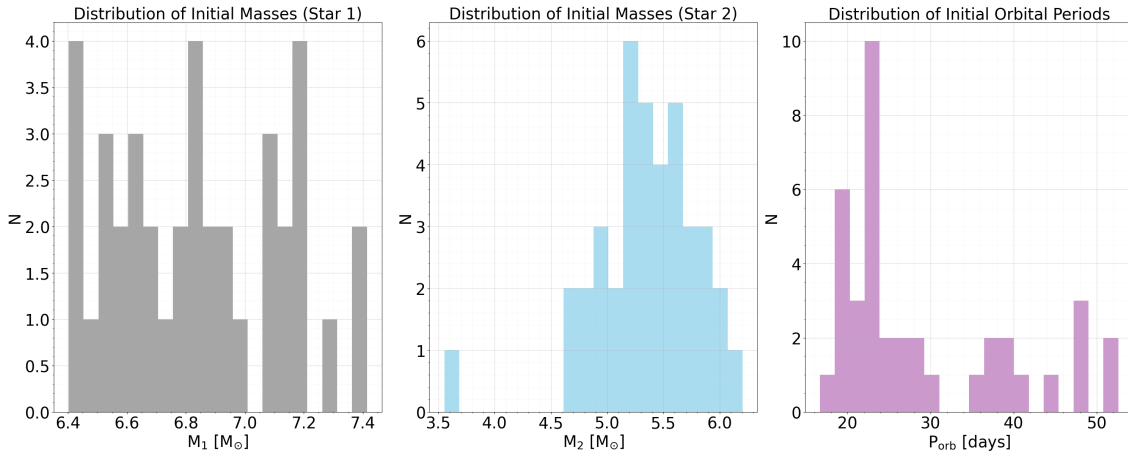
Figure 3.13: Initial Distributions of our varied parameters.

We first implemented a targeted filtering process of logical filters and boolean masks to identify AM CVn progenitor systems from a `POSYDON` population output. The primary filter selects systems where the primary star (S1) is a white dwarf (WD) and the secondary star (S2) is either H-rich with depleted central helium (HrCHeD) or a core hydrogen-burning star (CHB). The scheme deliberately excludes common alternate states like helium core burning secondaries (sHeCHeB), helium-depleted secondaries (sHeCHeD), or double white dwarf systems (S2 is WD). This selection has no orbital period constraint. This filter produces a subpopulation of $N = 61,900$. This initial population included all three main AM CVn formation channels, yet $N \approx 851$ formed from the He-star channel, $N \approx 425$ formed from the double WD channel, and fewer from the evolved CV channel. Many of these final systems, however, had a larger final $P_{orb} > 70$ minutes. To resolve the He-WD systems that have the most probable formation channel and to ensure that we have active mass transfer, we applied a secondary classification scheme. This approach identifies ultra-

compact binaries by selecting systems where the primary star (S1) is a white dwarf and the secondary (S2) is either a helium-burning star (stripped He Core He burning), a star with depleted central helium (stripped He Central He depleted), or another white dwarf. Critically, this scheme enforces a strict orbital period constraint of $P_{orb} \lesssim 60$ minutes, targeting only the most compact systems. We identify systems in active mass transfer from the secondary (RLO2) that haven't merged. From this classification, we found $N = 39$ systems that had active MT and survived CE2. Comparing our population's final $P_{\rm orb}$, we see that our simulation produced a distribution of AM CVn's fit within the period distribution of the current Observed AM CVn catalogue [48][3]
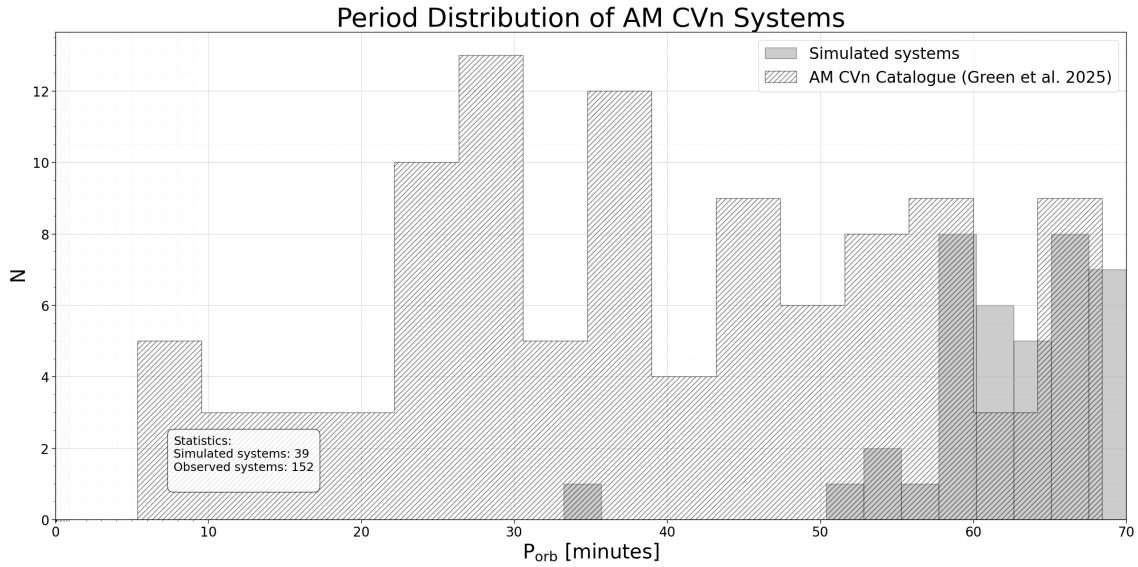
Figure 3.14: Final P_{orb} distribution of AM CVn's from the population data compared with the observed population [48].

In plotting the final orbital periods, we see a gap at $P_{\rm orb} \lesssim 35$ minutes. Not shown on the distribution is a large spike of models at 1 day. The absence of models of low orbital period as well as an abundance of models at 1 day, leads us to believe that a large portion of our simulations have systems that merged during CE1 and/or CE2. Looking at Figure 3.15, it is clear that most of our models may not have made it through CE1 and CE2 as the density of AM CVn-classified points of our plot is centered around regions which would suggest a higher likelihood of stable mass transfer at the end of the CO HeMS grid (i.e, 0.8). This

---

[3]The observed catalogue has more data points than our simulation results.

shows that the systems that survive CE2 begin undergoing stable mass transfer. That being said, the prominence of this high merger rate is likely either an issue with classification and the α_{CE} parameter, causing the orbit to shrink too much.

(a)

(b)

Figure 3.15: The final P_{orb} for a population of AM CVn's by mass ratio q at (a) at the beginning of the HMS-HMS grid and (b) at the beginning of the CO-HeMS grid.

Table 3.2: AM CVn Binary System Simulation Data | Population

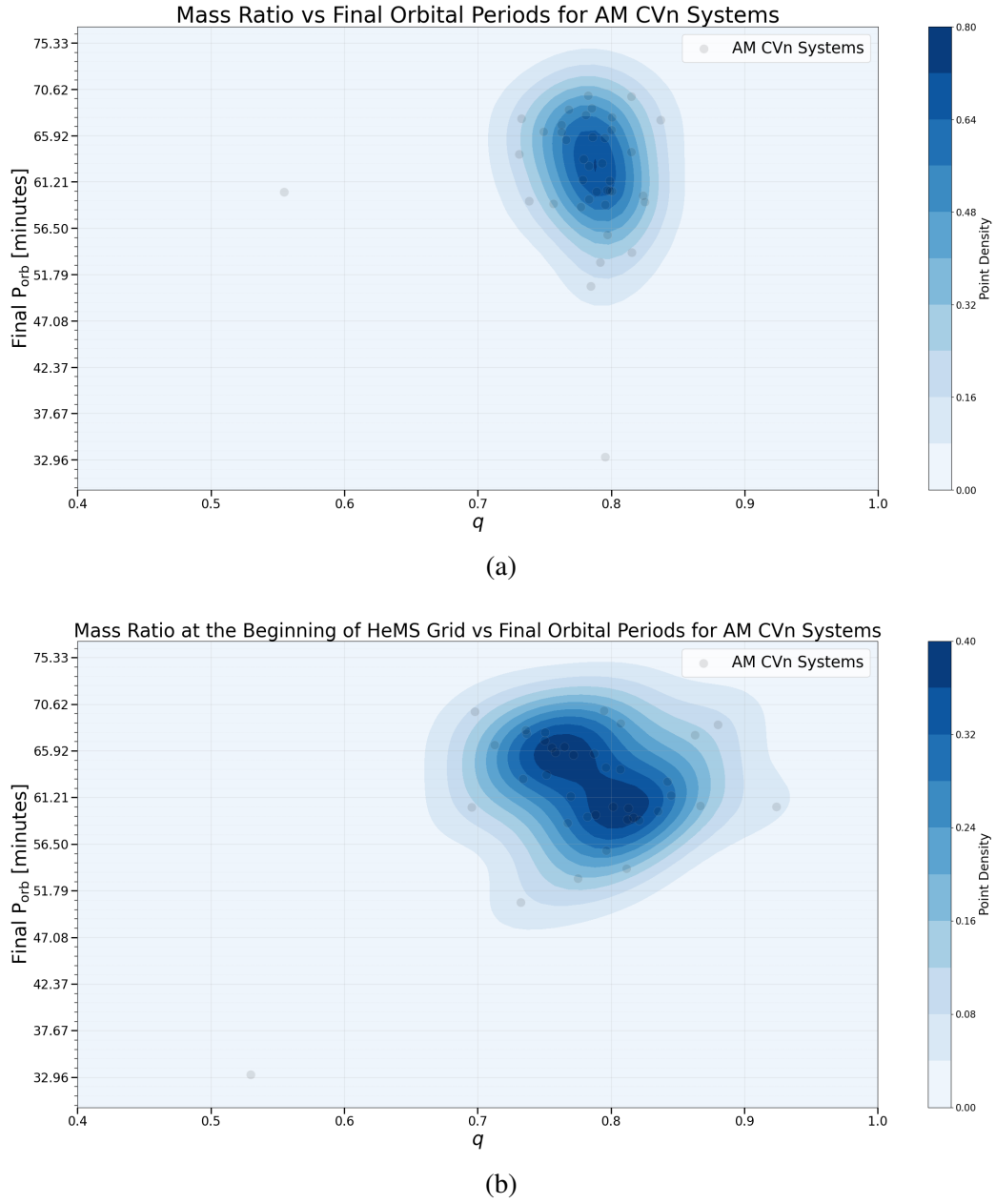| binary_index	state	S1_state	S1_mass	S2_state	S2_mass	orbital_period	eccentricity	step_names
24835	detached	WD	1.156596	stripped_He_non_burning	1.203368	0.041775	0.0	step_CE
52143	detached	WD	1.013582	stripped_He_Central_He_depleted	1.135503	0.044469	0.0	step_CE
92228	detached	WD	1.088775	stripped_He_Central_He_depleted	1.018667	0.046984	0.0	step_CE
106087	detached	WD	1.115061	stripped_He_Central_He_depleted	1.140227	0.041151	0.0	step_CE
121888	detached	WD	1.101619	stripped_He_Central_He_depleted	1.110703	0.046861	0.0	step_CE
138138	detached	WD	1.159024	stripped_He_non_burning	1.173904	0.040969	0.0	step_CE
146081	detached	WD	1.044929	stripped_He_Central_He_depleted	1.071512	0.048520	0.0	step_CE
207455	detached	WD	1.159132	stripped_He_non_burning	1.168396	0.047889	0.0	step_CE
235585	detached	WD	1.165287	stripped_He_non_burning	1.165432	0.045488	0.0	step_CE
246120	detached	WD	1.030551	stripped_He_non_burning	1.184863	0.047613	0.0	step_CE
256232	detached	WD	1.036404	stripped_He_Central_He_depleted	1.219769	0.046604	0.0	step_CE
275107	detached	WD	1.036774	stripped_He_non_burning	1.140587	0.043636	0.0	step_CE
320230	detached	WD	1.000230	stripped_He_Central_He_depleted	0.868730	0.036135	0.0	step_CE
351230	detached	WD	1.076877	stripped_He_non_burning	1.142386	0.042650	0.0	step_CE
351752	detached	WD	1.142716	stripped_He_Central_He_depleted	1.118172	0.040731	0.0	step_CE
356446	detached	WD	1.116132	stripped_He_Central_He_depleted	1.074659	0.044103	0.0	step_CE
356672	detached	WD	1.166439	stripped_He_non_burning	1.163319	0.041281	0.0	step_CE
384355	detached	WD	1.034857	stripped_He_Central_He_depleted	1.143139	0.047664	0.0	step_CE
432454	detached	WD	1.088816	stripped_He_Central_He_depleted	1.021490	0.047226	0.0	step_CE

Table 3.2: AM CVn Binary System Simulation Data | Population (continued)

binary_index	state	S1_state	S1_mass	S2_state	S2_mass	orbital_period	eccentricity	step_names
481970	detached	WD	1.158750	stripped_He_non_burning	1.170745	0.045602	0.0	step_CE
523512	detached	WD	1.100264	stripped_He_non_burning	0.870343	0.041627	0.0	step_CE
542460	detached	WD	1.066373	stripped_He_Central_He_depleted	1.131548	0.038618	0.0	step_CE
544770	detached	WD	1.055311	stripped_He_Central_He_depleted	1.140437	0.041671	0.0	step_CE
582725	detached	WD	1.120519	stripped_He_Central_He_depleted	1.143206	0.025275	0.0	step_CE
530322	detached	WD	1.117961	stripped_He_non_burning	1.208687	0.041916	0.0	step_CE
525278	detached	WD	1.052211	stripped_He_Central_He_depleted	0.931100	0.046174	0.0	step_CE
532005	detached	WD	1.011773	stripped_He_Central_He_depleted	1.245855	0.047063	0.0	step_CE
802618	detached	WD	1.150830	stripped_He_Central_He_depleted	1.079154	0.043620	0.0	step_CE
845564	detached	WD	1.063426	stripped_He_non_burning	0.523931	0.023075	0.0	step_CE
850117	detached	WD	1.121122	stripped_He_Central_He_depleted	1.144656	0.038795	0.0	step_CE
860375	detached	WD	1.164040	stripped_He_non_burning	1.207271	0.046376	0.0	step_CE
861751	detached	WD	1.005377	stripped_He_Central_He_depleted	1.131697	0.045580	0.0	step_CE
865744	detached	WD	1.047747	stripped_He_non_burning	1.452866	0.041863	0.0	step_CE
871904	detached	WD	1.032442	stripped_He_Central_He_depleted	1.137586	0.037521	0.0	step_CE
886151	detached	WD	1.129216	stripped_He_Central_He_depleted	1.153171	0.044608	0.0	step_CE
894245	detached	WD	1.135824	stripped_He_non_burning	1.290570	0.041540	0.0	step_CE
931713	detached	WD	1.101774	stripped_He_non_burning	1.197183	0.041063	0.0	step_CE
930562	detached	WD	1.166257	stripped_He_Central_He_depleted	1.020941	0.048522	0.0	step_CE

Table 3.2: AM CVn Binary System Simulation Data | Population (continued)

binary_index	state	S1_state	S1_mass	S2_state	S2_mass	orbital_period	eccentricity	step_names
934343	detached	WD	1.156835	stripped_He_non_burning	1.362617	0.046894	0.0	step_CE

Chapter 4

DISCUSSION AND CONCLUSION

Our preliminary findings indicate a population of 39 AM CVn-type binary systems for a toy galactic model of 10^6 stars with a burst formation rate. These are formed from an initial parameter range of 6.40 $M_\odot \lesssim M \lesssim$ 7.41 $M_\odot$, 16.68 days $\lesssim P_{\mathrm{orb}} \lesssim$ 52.5 days, $0.55 \lesssim q \lesssim 0.83$. Unlike the current analysis of AM CVn populations [36], who predicted AM CVn systems with $P_{orb} \lesssim 40$ days to be $\approx 112,000$ out of a galactic population, our initial population is much smaller. So in expanding this study, a larger set of models would provide us with more resolution upon which to train our classifiers and interpolator. With higher resolution in our detailed grids, we can be sure we're properly sampling the entire parameter space. With a sparse grid, we miss significant islands of stable mass transfer or other cases that could produce AM CVn. Moreover, our galaxy is home to a wide range of metallicities as the compositions of stars change with distance from the galactic center, therefore, another dimension to add to the population modeling is running the stellar evolution models for varying metallicities. In future work, we intend to factor in a more precise classification as well as the code that was used in [36] for a more complete analysis.

One key constraint on the ability for AM CVn's to reach such a short orbital period is the α_{CE} parameter. We find that many of our systems merge right after CE1 and discontinue their evolution or merge after CE2. We see this in our distribution of q vs final period. This can be attributed to an over-efficient α_{CE} parameter within the `POSYDON` code, which is more efficient than in nature. If too many systems merge too quickly, they won't ever reach the mass transfer that categorizes an AM CVn. For instance, varying the α_{CE} parameter at solar metallicity would be a first step in determining proper α_{CE} for our models. We can also run our models for a range of metallicity and α_{CE}, as has been done with the formation of Neutron star mergers [29], can lead us to a better understanding of how the uncertainties in modeling the CE phase of binary evolution impact the predicted AM CVn population.

Modes of angular momentum transport, such as magnetic braking, also play a crucial role in the shrinking of the binary separation in early stages of evolution [35]. This orbital shrinking caused by slowed rotation from the surface magnetic field, coupled with stellar wind, exerting a torque on the star is key to producing AM CVn's and we are vastly limited in the origins of stellar magnetic fields and how to model their evolution. Moreover, the theory surrounding stellar spin down [49] continues to see development from recent 2D and 3D simulations [50], as well as observational data from GAIA and TESS [51] reveal details on the magnetized stellar winds driving the angular momentum loss of low-mass stars. These affects are necessary to take into account to correctly model AM CVn's. In future work, we intend to resolve the issue of early mergers after CE1, which should leave us with more systems where the secondary star is HMS and the primary is a WD with a tight orbit. These systems would be heavily effected by magnetic braking and the tight orbits are strongly coupled through tides. The interactions between magnetic braking and tides leads to substantial angular momentum loss from the binary leading to mass transfer. There are many magnetic braking prescriptions in the literature that a following study can test the efficiency of in producing populations of AM CVn. These AM CVn systems would likely be the result of orbital collapse under magnetic braking, producing the hydrogen AM CVn in the evolved cataclysmic variable channel [52]. Further studies which take into account several magnetic braking prescriptions as well as focus on a range of values of α_{CE}, are necessary to constrain our stellar evolution models will ascertain a more accurate population of AM CVn systems.

BIBLIOGRAPHY

[1]B. e. a. Abbott, "Gw150914: first results from the search for binary black hole coalescence with advanced ligo", Physical Review D **93**, `10.1103/physrevd.93.122003` (2016).

[2]European Space Agency, *LISA factsheet*, Website, Adopted on 25 January 2024, 2024.

[3]M. V. Zombeck, *Handbook of space astronomy and astrophysics*, 3rd ed. (Cambridge University Press, 2007).

[4]B. Paxton et al., "Modules for Experiments in Stellar Astrophysics (MESA)", **192**, 3, 3 (2011).

[5]B. Paxton et al., "MODULES FOR EXPERIMENTS IN STELLAR ASTROPHYSICS (MESA): BINARIES, PULSATIONS, AND EXPLOSIONS", en, The Astrophysical Journal Supplement Series **220**, 15 (2015).

[6]B. Paxton et al., "Modules for Experiments in Stellar Astrophysics (MESA): Convective Boundaries, Element Diffusion, and Massive Star Explosions", en, The Astrophysical Journal Supplement Series **234**, arXiv:1710.08424 [astro-ph], 34 (2018).

[7]B. Paxton et al., "Modules for Experiments in Stellar Astrophysics (MESA): Pulsating Variable Stars, Rotation, Convective Boundaries, and Energy Conservation", en, The Astrophysical Journal Supplement Series **243**, arXiv:1903.01426 [astro-ph], 10 (2019).

[8]R. Kippenhahn and A. Weigert, *Stellar Structure and Evolution* (1990).

[9]S. Chandrasekhar, *An introduction to the study of stellar structure* (1939).

[10]B. W. Carroll and D. A. Ostlie, *An introduction to modern astrophysics*, 2nd ed. (Cambridge University Press, 2017).

[11]A. C. Beyer and R. J. White, "The Kraft Break Sharply Divides Low-mass and Intermediate-mass Stars", **973**, 28, 28 (2024).

[12]Cantiello, M. and Langer, N., "Thermohaline mixing in evolved low-mass stars", AA **521**, A9 (2010).

[13]Käpylä, P. J., "Star-in-a-box simulations of fully convective stars", AA **651**, A66 (2021).

[14]D. J. Griffiths and D. F. Schroeter, *Introduction to quantum mechanics*, Third edition (Cambridge University Press, Cambridge ; New York, NY, 2018), pp. 217–219.

[15]O. Pols, *Binaries and stellar evolution*, Lecture Notes for Utrecht University MSc Course, Unpublished lecture notes, Feb. 2015.

[16]G. Meynet, J. .-. Mermilliod, and A. Maeder, "New dating of galactic open clusters.", **98**, 477–504 (1993).

[17]O. R. Pols et al., "Stellar evolution models for Z = 0.0001 to 0.03", **298**, 525–536 (1998).

[18]S. Höfner and H. Olofsson, "Mass loss of stars on the asymptotic giant branch. Mechanisms, models and measurements", **26**, 1, 1 (2018).

[19] T. M. Tauris and E. P. J. v. d. Heuvel, *Physics of binary star evolution: from stars to x-ray binaries and gravitational wave sources* (Princeton University Press, 2023).

[20] A. S. Hamers and F. Dosopoulou, "An analytic model for mass transfer in binaries with arbitrary eccentricity, with applications to triple-star systems", The Astrophysical Journal **872**, 119 (2019).

[21] G. E. Soberman and E. S. Phinney, "Stability criteria for mass transfer in binary stellar evolution", en,

[22] K. D. Temmink et al., "Coping with loss: Stability of mass transfer from post-main-sequence donor stars", en, Astronomy & Astrophysics **669**, A45 (2023).

[23] M. Livio and N. Soker, "The common envelope phase in the evolution of binary stars", en, The Astrophysical Journal **329**, 764 (1988).

[24] O. De Marco et al., "On the α formalism for the common envelope interaction", **411**, 2277–2292 (2011).

[25] M. U. Kruckow et al., "Common-envelope ejection in massive binary stars: Implications for the progenitors of GW150914 and GW151226", en, Astronomy & Astrophysics **596**, A58 (2016).

[26] D. Kousiounelos, S. Gossage, and V. Kalogera, "On The Visualization of Binary Stellar Evolution for POSYDON", in American astronomical society meeting abstracts, Vol. 243, American Astronomical Society Meeting Abstracts,
Wrote a code, `binarystory` which generated the visualizations used in this paper. (Feb. 2024), p. 205.10.

[27] M. Gallegos-Garcia et al., "Binary Black Hole Formation with Detailed Modeling: Stable Mass Transfer Leads to Lower Merger Rates", **922**, 110, 110 (2021).

[28] P. Marchant et al., "The role of mass transfer and common envelope evolution in the formation of merging binary black holes", **650**, A107, A107 (2021).

[29] M. Gallegos-Garcia, C. P. L. Berry, and V. Kalogera, "Evolutionary Origins of Binary Neutron Star Mergers: Effects of Common Envelope Efficiency and Metallicity", **955**, 133, 133 (2023).

[30] T. Fragos et al., "POSYDON: A General-Purpose Population Synthesis Code with Detailed Binary-Evolution Simulations", en, The Astrophysical Journal Supplement Series **264**, arXiv:2202.05892 [astro-ph], 45 (2023).

[31] J.-E. Solheim, "AM CVn Stars: Status and Challenges", en, Publications of the Astronomical Society of the Pacific **122**, 1133–1163 (2010).

[32] A. F. Lanza, "Internal magnetic fields, spin-orbit coupling, and orbital period modulation in close binary systems", en, Monthly Notices of the Royal Astronomical Society, stz3135 (2019).

[33] G. Ramsay et al., "Physical properties of AM CVn stars: New insights from *Gaia* DR2", en, Astronomy & Astrophysics **620**, A141 (2018).

[34] S. Scaringi et al., "Cataclysmic variables are a key population of gravitational wave sources for LISA", en, Monthly Notices of the Royal Astronomical Society: Letters **525**, arXiv:2307.02553 [astro-ph, physics:gr-qc], L50–L55 (2023).

[35] S. Gossage, V. Kalogera, and M. Sun, "Magnetic Braking with MESA Evolutionary Models in the Single Star and Low-mass X-Ray Binary Regimes", en, The Astrophysical Journal **950**, 27 (2023).

[36] W.-M. Liu, L. Yungelson, and A. Kuranov, "He-star donor AM CVn stars and their progenitors as LISA sources", en, Astronomy & Astrophysics **668**, arXiv:2210.08434 [astro-ph], A80 (2022).

[37] T. L. S. Wong and L. Bildsten, "Mass Transfer and Stellar Evolution of the White Dwarfs in AM CVn Binaries", en, The Astrophysical Journal **923**, 125 (2021).

[38] W.-M. Liu, L. Yungelson, and A. Kuranov, "He-star donor am cvn stars and their progenitors as lisa sources", Astronomy amp; Astrophysics **668**, A80 (2022).

[39] P. J. Carter et al., "A search for the hidden population of AM CVn binaries in the Sloan Digital Sky Survey", en, Monthly Notices of the Royal Astronomical Society **429**, 2143–2160 (2013).

[40] L. Bildsten et al., "The Thermal State of the Accreting White Dwarf in AM Canum Venaticorum Binaries", en, The Astrophysical Journal **640**, 466–473 (2006).

[41] P. P. Eggleton, "The evolution of low mass stars", **151**, 351 (1971).

[42] E. National Academies of Sciences and Medicine, *Pathways to Discovery in Astronomy and Astrophysics for the 2020s* (The National Academies Press, Washington, DC, 2023).

[43] I. Brott et al., "Rotating massive main-sequence stars: I. Grids of evolutionary models and isochrones", en, Astronomy & Astrophysics **530**, A115 (2011).

[44] J. Choi et al., "MESA ISOCHRONES AND STELLAR TRACKS (MIST). I. SOLAR-SCALED MODELS", en, The Astrophysical Journal **823**, 102 (2016).

[45] E. H. Anders and M. G. Pedersen, "Convective Boundary Mixing in Main-Sequence Stars: Theory and Empirical Constraints", en, Galaxies **11**, 56 (2023).

[46] L. Ferrario et al., "The open-cluster initial-final mass relationship and the high-mass tail of the white dwarf distribution", **361**, 1131–1135 (2005).

[47] M. Green, *Private communication*, Personal communication, University of Oklahoma, Apr. 2025.

[48] M. Green, *A catalogue of all known mass-transferring ultracompact binary systems*, 2025.

[49] S. P. Matt et al., "The Mass-dependence of Angular Momentum Evolution in Sun-like Stars", **799**, L23, L23 (2015).

[50] C. Garraffo, J. J. Drake, and O. Cohen, "The missing magnetic morphology term in stellar rotation evolution", Astronomy amp; Astrophysics **595**, A110 (2016).

[51] Y. L. Lu et al., "An abrupt change in the stellar spin-down law at the fully convective boundary", Nature Astronomy **8**, 223–229 (2024).

[52] D. Belloni and M. R. Schreiber, "Reversing the verdict: Cataclysmic variables could be the dominant progenitors of AM CVn binaries after all", **678**, A34, A34 (2023).